Electronic Supporting Information

High Seebeck Coefficient from Isolated Oligo-Phenyl Arrays on Single Layered Graphene via Stepwise Assembly

Xintai Wang,[a'*,†] Ali Ismael,[b,c*,†] Bashayr Alanazi,[b,d,†] Alaa Al-Jobory,[b,e] Junsheng Wang,[a*] and Colin J. Lambert[b*]

Contents

1. DFT and Transport Simulations

In this section, geometries, electronic structures and transport properties of all junctions are presented. The main aim in this study is to examine the change in transport properties when molecular monolayer or molecule/ZnTPP bilayer is inserted in Gr-Au junction for eight different mono or bilayers.

1.1 Optimised DFT Structures of Isolated Molecular-scale Structures

Using the density functional code SIESTA[1], the optimum geometries of the isolated molecules were obtained by relaxing the molecules until all forces on the atoms were less than 0.01 eV / Å.[4,5] A double-zeta plus polarization orbital basis set, norm-conserving pseudopotentials, an energy cut-off of 250 Rydbergs defining the real space grid were used and the local density approximation (GGA)[2-4] was chosen as the exchange correlation functional. The basic building blocks **1-7** of this study are shown in Fig. S1. Zinc Tetraphenyl Porphyrin (ZnTPP, molecule **4**), combines with **5**, **6** and **7** to form bilayers.

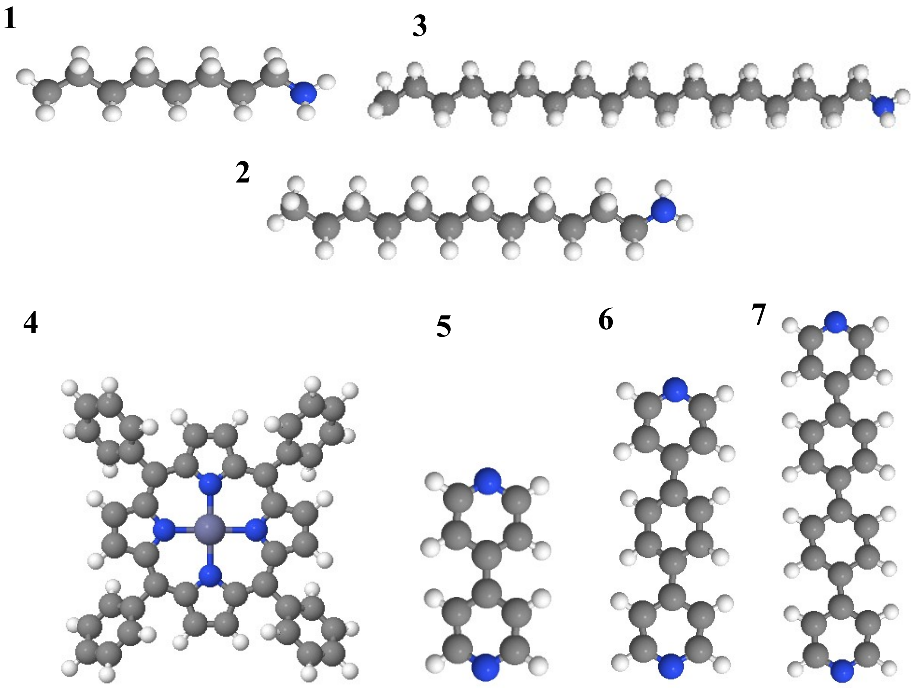

Figure S1: Simulated structures of monolayers **1-3** and component of bilayers **4-7**.

The following 3 molecular structures were assembled by combining the ZnTPP with **5**, **6** and **7** (Fig. S1), and then allowing the system to become fully relaxed to form bilayers as shown in Fig. S2.

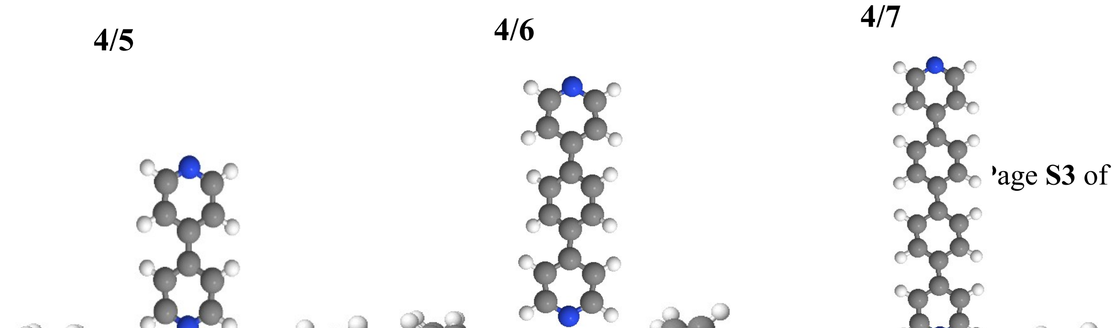

Figure S2: Schematic illustrations of isolated molecules **4-7** attached to the ZnTPP to form bilayers: **4/5, 4/6** and **4/7**.

1.2 Frontier molecular orbitals

To have a good understanding of electronic properties, the frontier orbital of studied molecules: highest occupied molecular orbitals (HOMO) and lowest unoccupied orbitals (LUMO), in addition to (HOMO+1), and (LUMO-1), along with their energies are investigated. we investigate first the monolayers and then bilayers as shown in Figs. S3-S12. The blue and red colours represent the positive and negative orbital amplitude.

1.2.1 monolayer 1

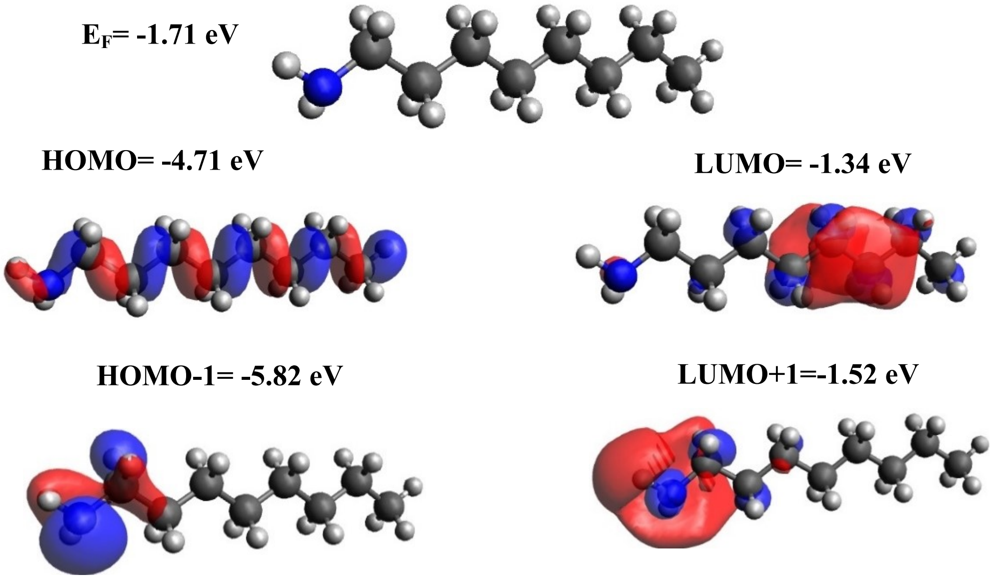

Figure S3: Wave function for monolayer **1**. Top panel: fully optimised geometry of **1**. Lower panel: HOMO, LUMO, HOMO-1, LUMO+1 of monolayer **1**, along with their energies.

1.2.2 monolayer 2

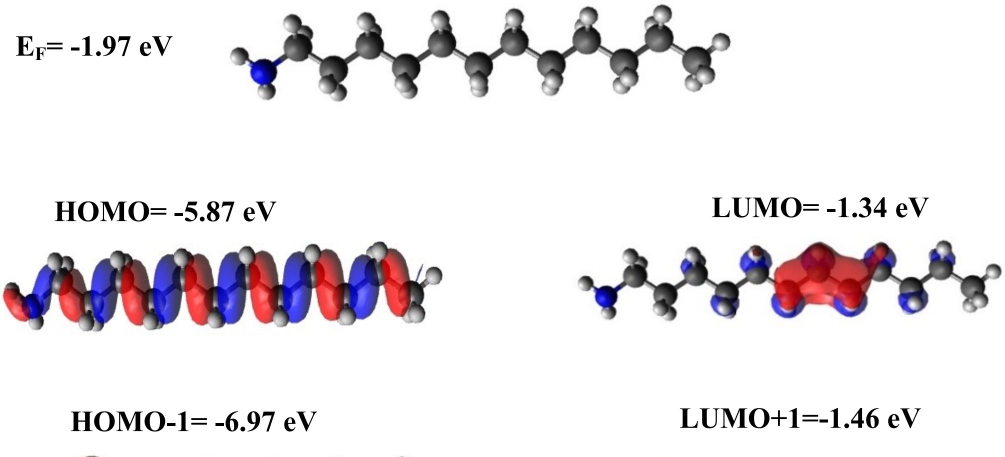

Figure S4: Wave function for monolayer **2.** Top panel: fully optimised geometry of **2**. Lower panel: HOMO, LUMO, HOMO-1, LUMO+1 of monolayer **2**, along with their energies.

1.2.3 monolayer 3

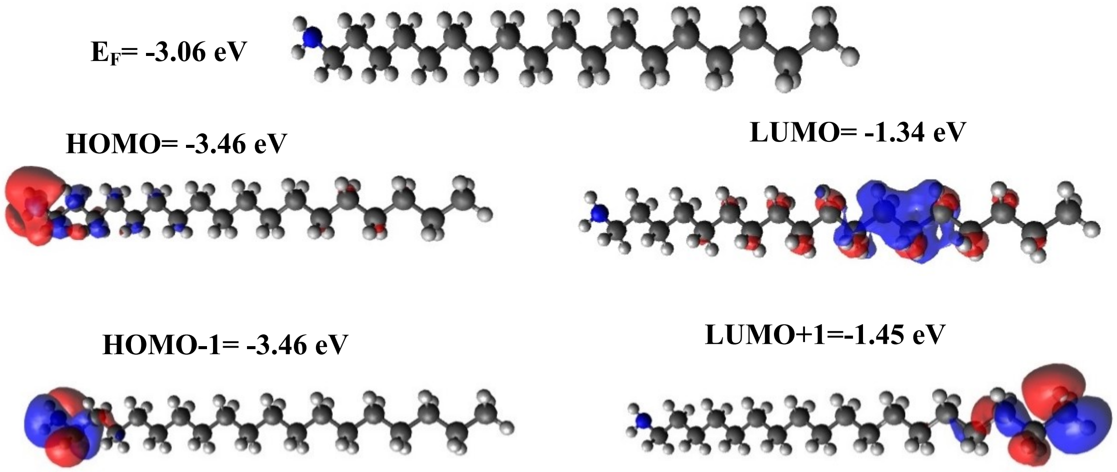

Figure S5: Wave function for monolayer **3.** Top panel: fully optimised geometry of **3**. Lower panel: HOMO, LUMO, HOMO-1, LUMO+1 of monolayer **3**, along with their energies.

1.2.4 monolayer 4

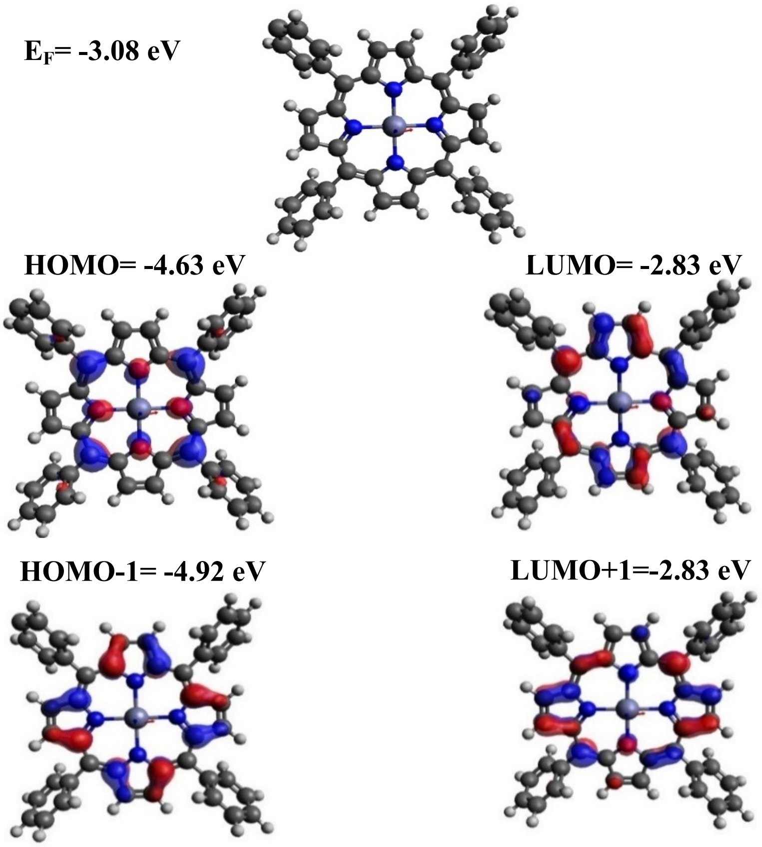

Figure S6: Wave function for monolayer **4.** Top panel: fully optimised geometry of **4**. Lower panel: HOMO, LUMO, HOMO-1, LUMO+1 of monolayer **4,** along with their energies.

1.2.5 monolayer 5

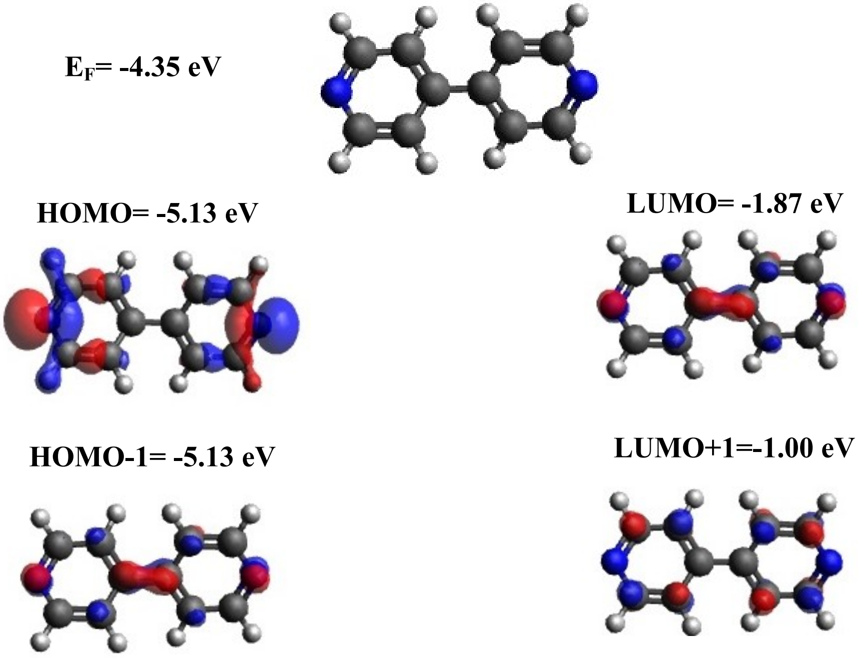

Figure S7: Wave function for monolayer **5.** Top panel: fully optimised geometry of **5**. Lower panel: HOMO, LUMO, HOMO-1, LUMO+1 of monolayer **5**, along with their energies.

1.2.6 monolayer 6

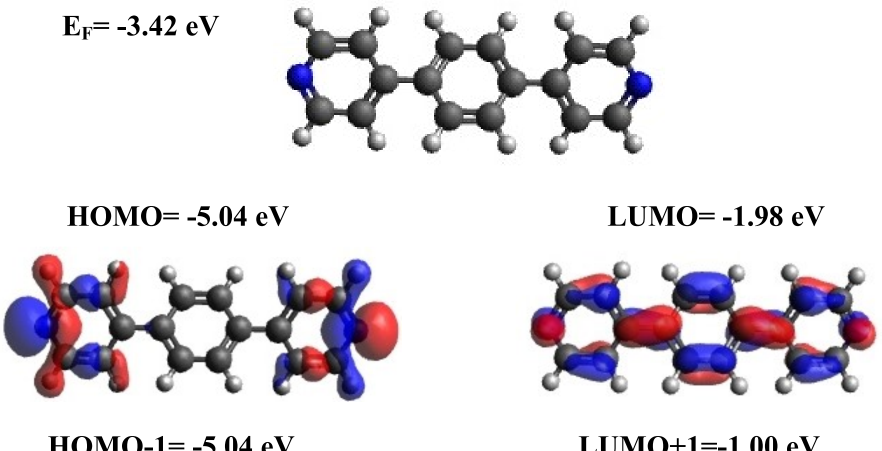

Figure S8: Wave function for monolayer **6.** Top panel: fully optimised geometry of **6**. Lower panel: HOMO, LUMO, HOMO-1, LUMO+1 of monolayer **6**, along with their energies.

1.2.7 monolayer 7

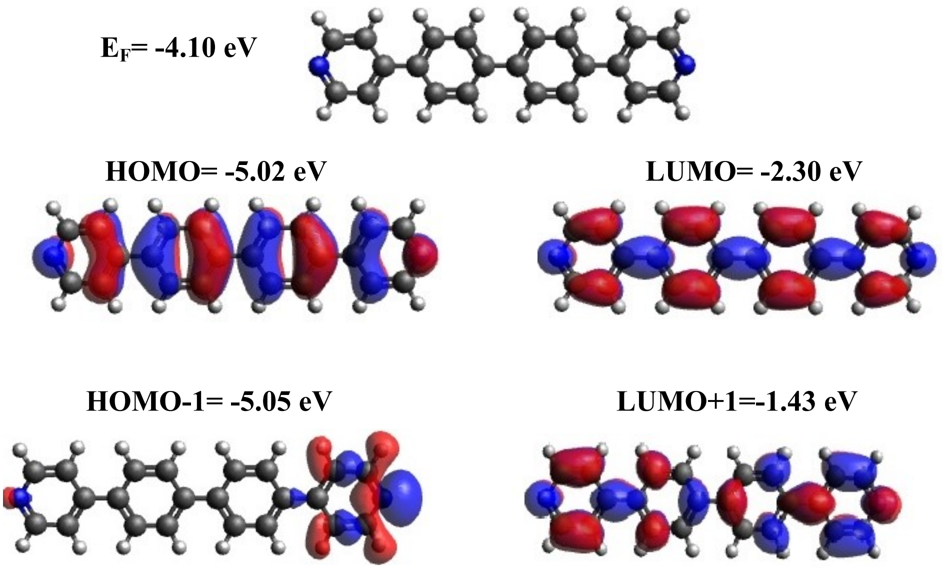

Figure S9: Wave function for

monolayer **7.** Top panel: fully optimised geometry of **7**. Lower panel: HOMO, LUMO, HOMO-1, LUMO+1 of monolayer **7**, along with their energies.

.

The next step is the bilayers, which are formed from two mono layers mainly ZnTTP **(4),** with **5, 6** and **7,** and as follows:

1.2.8 bilayer 1

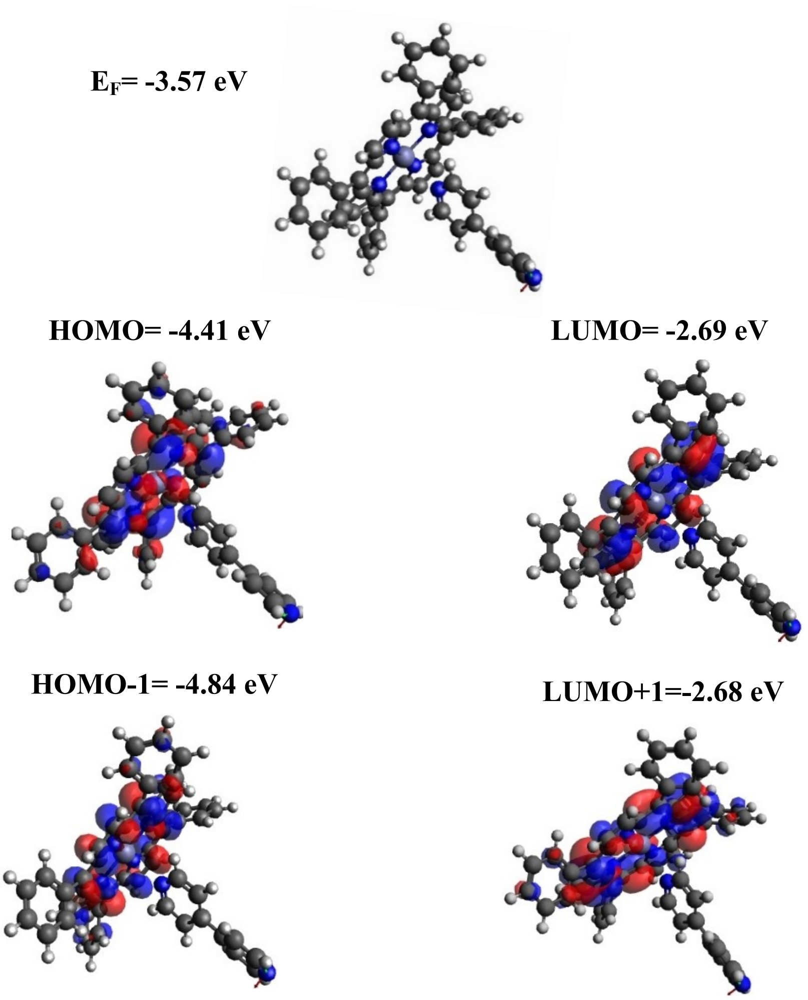

Figure S10: Wave function for bilayer **1.** Top panel: fully optimised geometry of **1**. Lower panel: HOMO, LUMO, HOMO-1, LUMO+1 of bilayer **1**, along with their energies.

.

1.2.9 bilayer 2

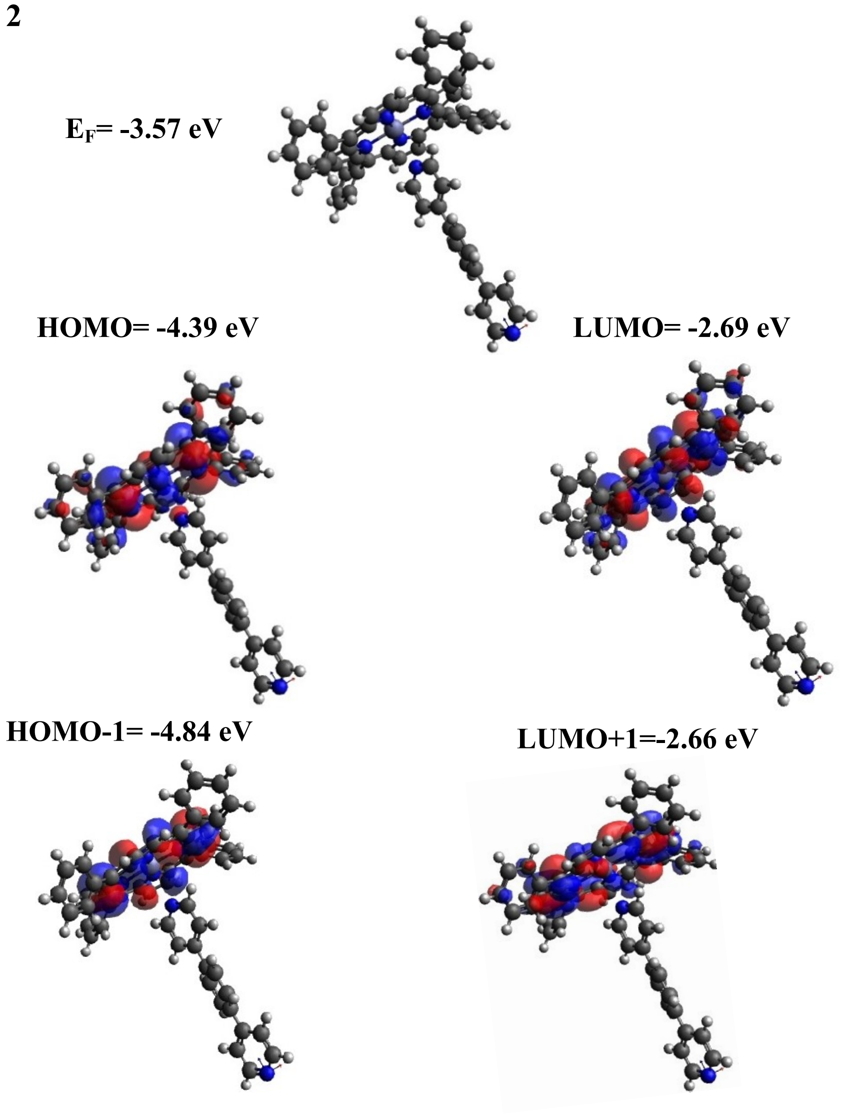

Figure S11: Wave function for bilayer **2.** Top panel: fully optimised geometry of **2**. Lower panel: HOMO, LUMO, HOMO-1, LUMO+1 of bilayer **2**, along with their energies.

.

1.2.10 bilayer 3

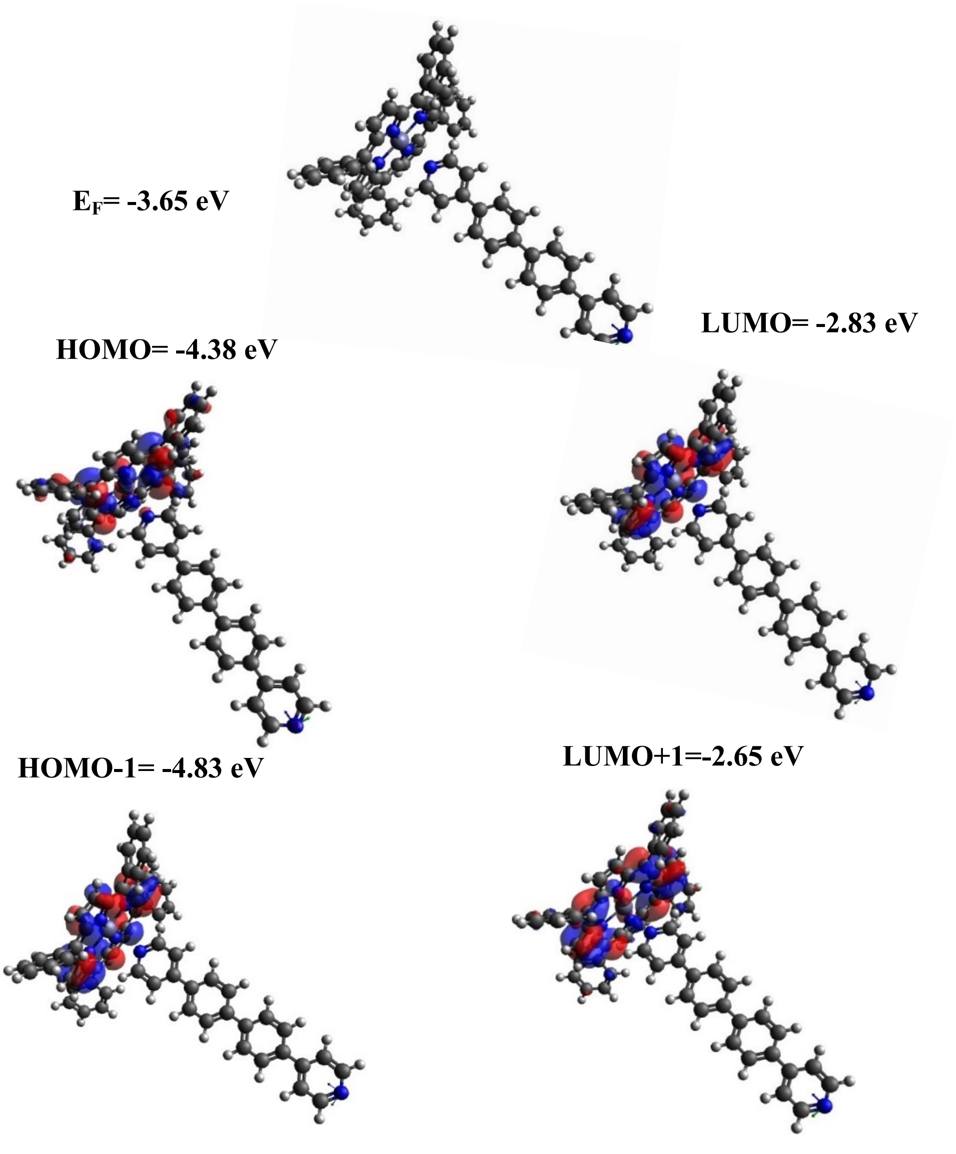

Figure S12:
Wave

function for bilayer **3.** Top panel: fully optimised geometry of **3**. Lower panel: HOMO, LUMO, HOMO-1, LUMO+1 of bilayer **3**, along with their energies.

1.3 Binding energies

To calculate the optimum binding distance between any two components, we used DFT and the counterpoise method, which removes basis set superposition errors (BSSE). The binding distance d is defined as the distance between compound 1 and compound 2. Here, compound **1** is defined as entity A and compound **2** as entity B. The ground state energy of the total system is calculated using SIESTA and is denoted E^{AB}_{AB}. The energy of each entity is then calculated in a fixed basis, which is achieved using ghost atoms in SIESTA. Hence, the energy of the individual **1** in the presence of the fixed basis is defined as E^{AB}_{A} and for the gold as E^{AB}_{B}. The binding energy is then calculated using the following equation[5-7]:

$$Binding\ Energy = E^{AB}_{AB} - E^{AB}_{A} - E^{AB}_{B} \tag{S1}$$

1.3.1 Binding energy on a gold surface

In this section, the optimum distance between the Au electrode and different molecules was calculated and as follows:

1.3.1.1 Au-CH_2

The optimum distance between the Au electrode and CH_2 anchor is found to be about 2.3 Å, at approximately -1.0 eV as shown in Fig. S13.

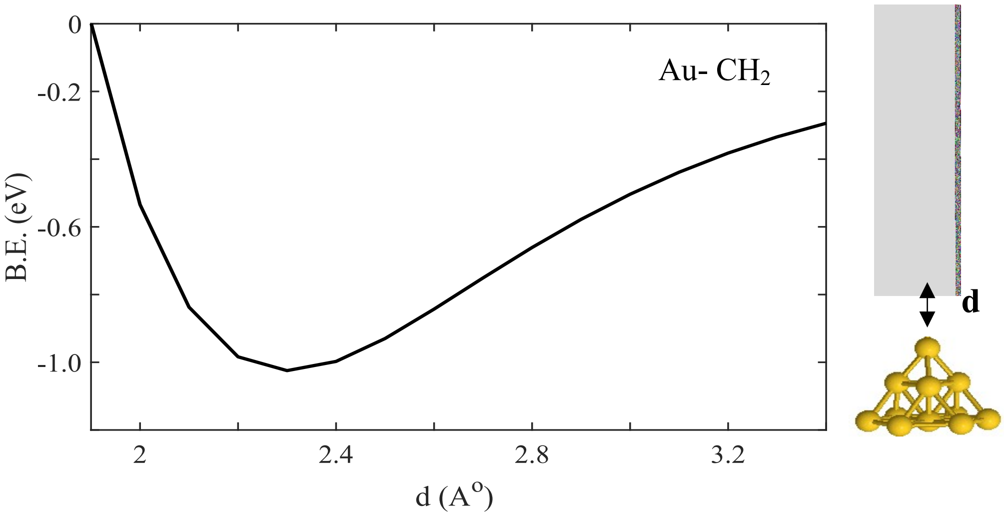

Figure S13: Right panel: represents molecule **1** binding to a gold ad-atom. Left panel: Binding energy as a function of the optimum binding distance *d*, where *d* is found to be approximately 2.3 Å, and binding energy B.E= 1.0 eV.

1.3.1.2 Au-Py

The optimum distance between the Au electrode and pyridyl anchor is found to be about 2.3 Å, at approximately -0.4 eV as shown in Fig. S14.

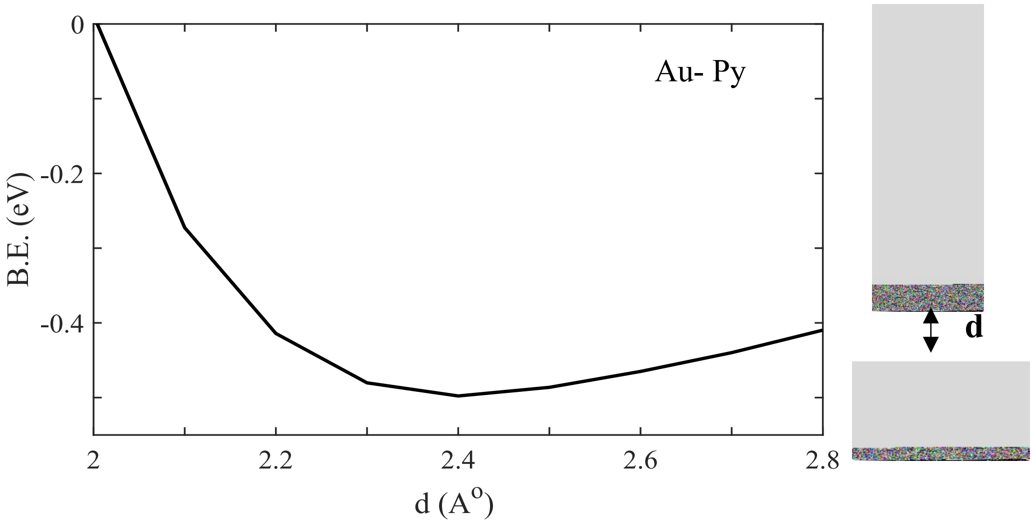

Figure S14: Right panel: represents molecule **7** binding to a gold ad-atom. Left panel: Binding energy as a function of the optimum binding distance *d*, where *d* is found to be approximately 2.3 Å, and binding energy B.E= 0.4 eV.

1.3.1.3 Au-ZnTTP

The optimum distance between the Au electrode and pyridyl anchor is found to be about 2.9 Å, at approximately -0.5 eV as shown in Fig. S15.

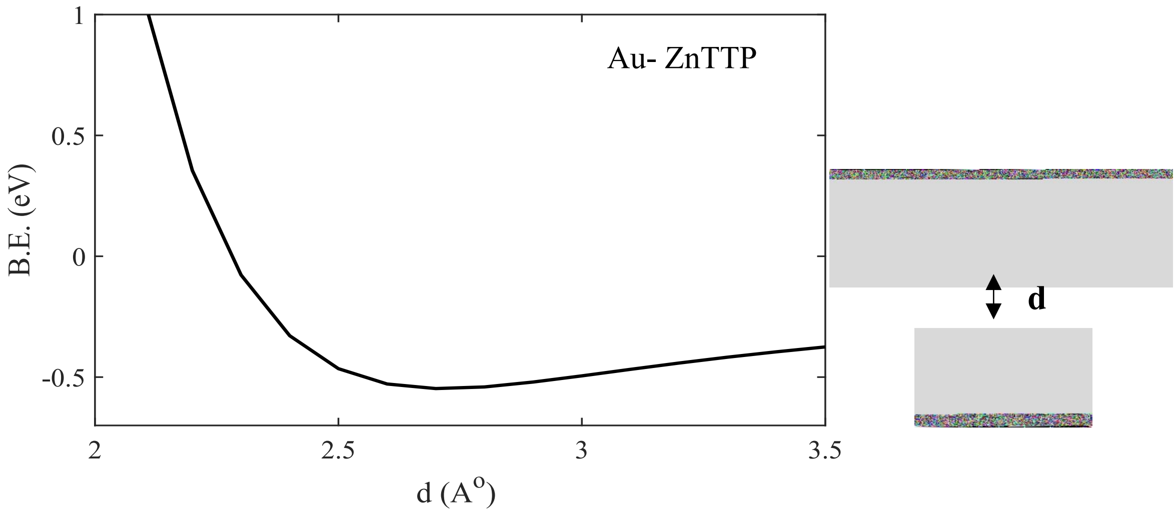

Figure S15: Right panel: represents ZnTTP molecule binding to gold ad-atom. Left panel: Binding energy as a function of the optimum binding distance *d*, where *d* is found to be approximately 2.9 Å, and binding energy B.E= 0.5 eV.

1.3.2 Binding energy on graphene sheet

In this section, the optimum distance between a Gr sheet and different molecules was calculated and as follows:

1.3.2.1 Gr-NH_2

The optimum distance between the Au electrode and pyridyl anchor is found to be about 3.4 Å, at approximately -0.2 eV as shown in Fig. S16.

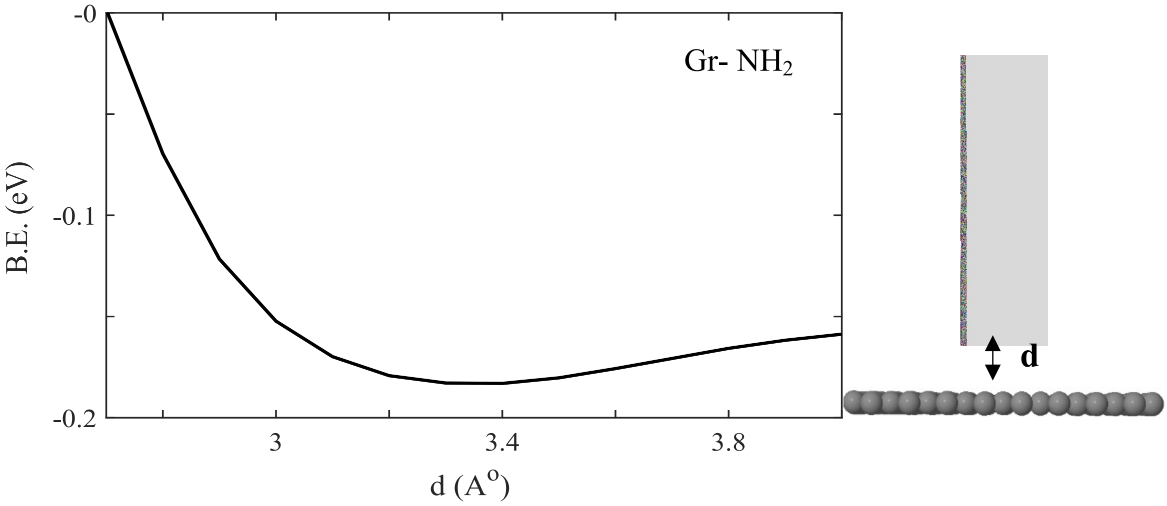

Figure S16: Right panel: represents molecule **1** binding to graphene sheet. Left panel: Binding energy as a function of the optimum binding distance *d*, where *d* is found to be approximately 3.4 Å, and binding energy B. E= 0.20 eV.

1.3.2.2 Gr-ZnTTP

The optimum distance between the Au electrode and pyridyl anchor is found to be about 4.0 Å, at approximately -0.2 eV as shown in Fig. S17.

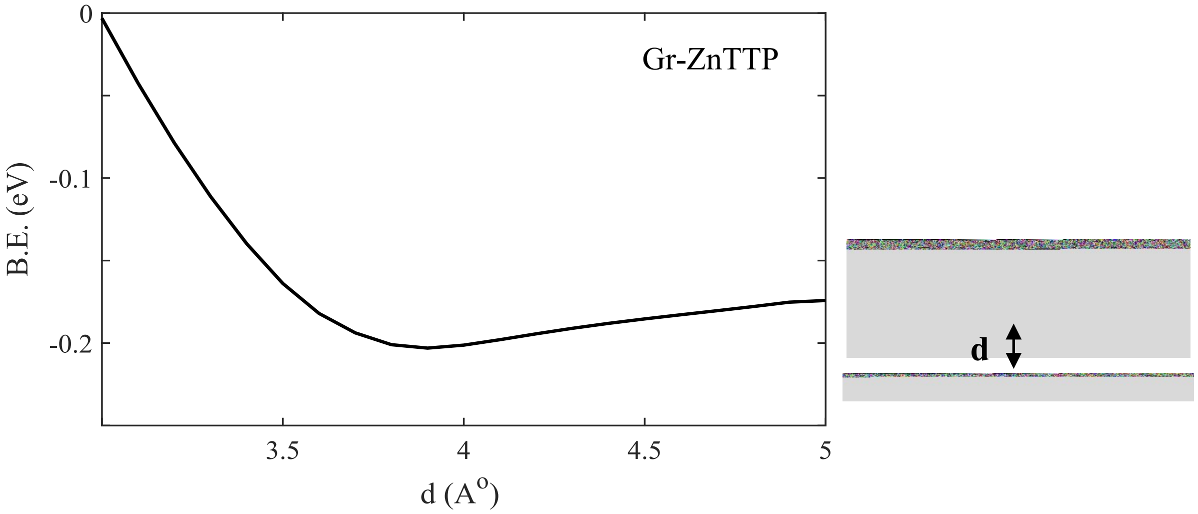

Figure S17: Right panel: represents the ZnTTP molecule binding to graphene sheet. Left panel: Binding energy as a function of the optimum binding distance *d*, where *d* is found to be approximately 4.0 Å, and binding energy B.E= 0.2 eV.

1.3.2.3 Py-ZnTTP

The optimum distance between the ZnTTP molecule and pyridyl anchor is found to be about 2.3 Å, at approximately -0.5 eV as shown in Fig. S18.

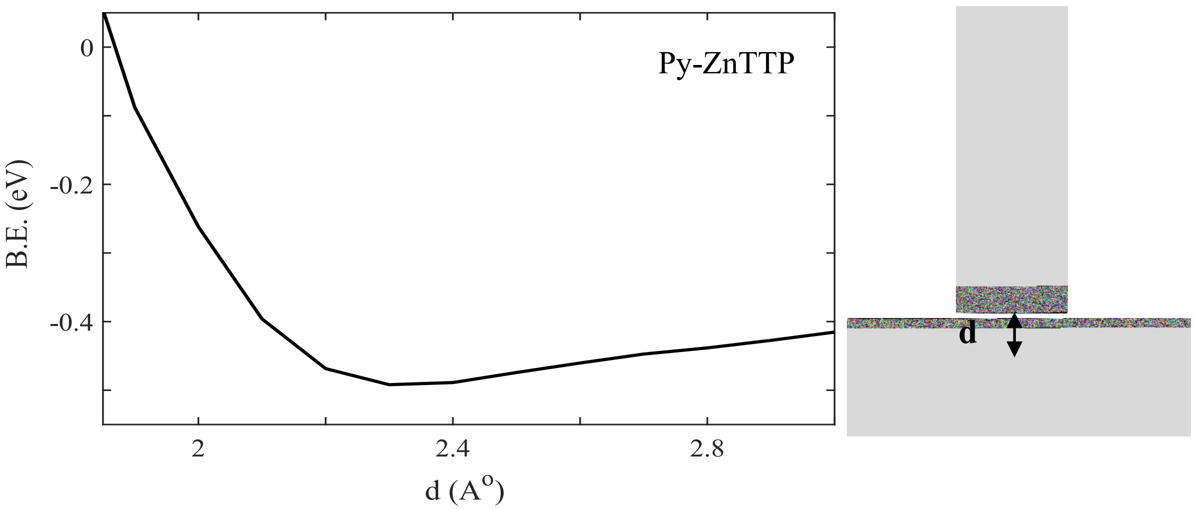

Figure S18: Right panel: represents the ZnTTP binding to molecule **7** through Zn atom. Left panel: Binding energy as a function of the optimum binding distance *d*, where *d* is found to be approximately 2.3 Å, and binding energy B.E= 0.5 eV.

1.3.2.4 Gr-Py-ZnTTP

The optimum distance between bilayer and graphene sheet anchor is found to be about 4.0 Å, at approximately -0.15 eV as shown in Fig. S19.

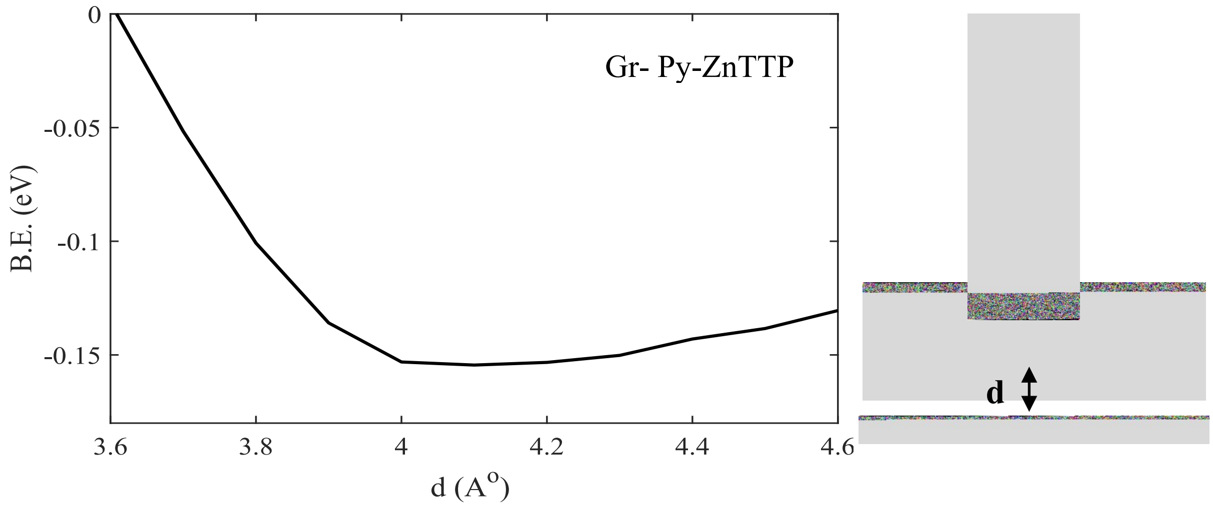

Figure S19: Right panel: represents bilayer **3** binding to graphene sheet. Left panel: Binding energy as a function of the optimum binding distance *d*, where *d* is found to be approximately 4.0 Å, and binding energy B.E= 0.15 eV.

Table S1: Summarises all the binding energies (B.E), and optimum distances (*d*), calculations for mono/bilayers that bind to gold or graphene sheet at different contact points.

Contact point	*d* (Å)	B.E (eV)
Au-CH_2	2.3	1.00
Au-Py	2.3	0.40
Au-ZnTTP	2.9	0.50
Gr-NH_2	3.4	0.20
Gr-ZnTTP	4.0	0.20
ZnTTP-Py	2.3	0.50
Gr-bilayer	4.0	0.15

Table S1, represents the optimum separation distance and binding energy for seven different anchor groups bind to each other to form bilayer or either to graphene or gold electrodes. The comparison between them shows that anchors are coupled to Au more strongly compared to Gr up to 5 times stronger and the optimum distance is larger.

1.4 Optimised DFT Structures of Compounds in their Junctions

Using the optimized structures and geometries for the compounds obtained as described above, we again employed the SIESTA code to calculate self-consistent optimized geometries, ground state Hamiltonians and overlap matrix elements for each graphene-molecule-gold junction. This section includes alkyl chains **1-3** and phenyl ring derivatives **4-7** with different anchor groups including pyridyl, CH_2, amine and large anchor such as ZnTTP. These mono or bilayers sandwiched between two electrodes first, then between gold and single layer graphene sheet (SLG).

1.4.1 Gold-gold simulations

In this section, the studied systems are sandwiched between to two gold electrodes for both monolayers involving **1, 2, 3**, Gr and **4**. As shown in Fig. S20.

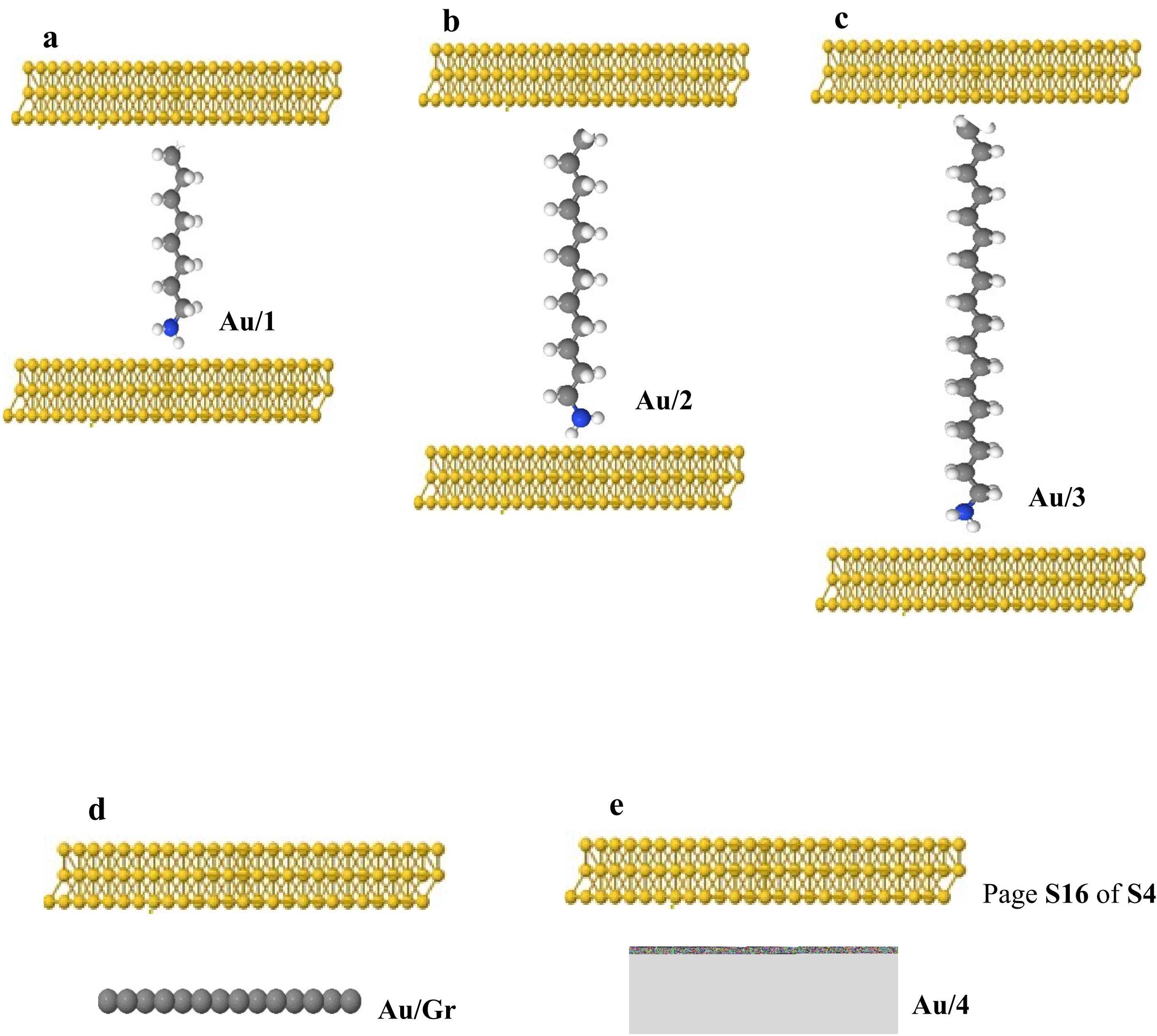

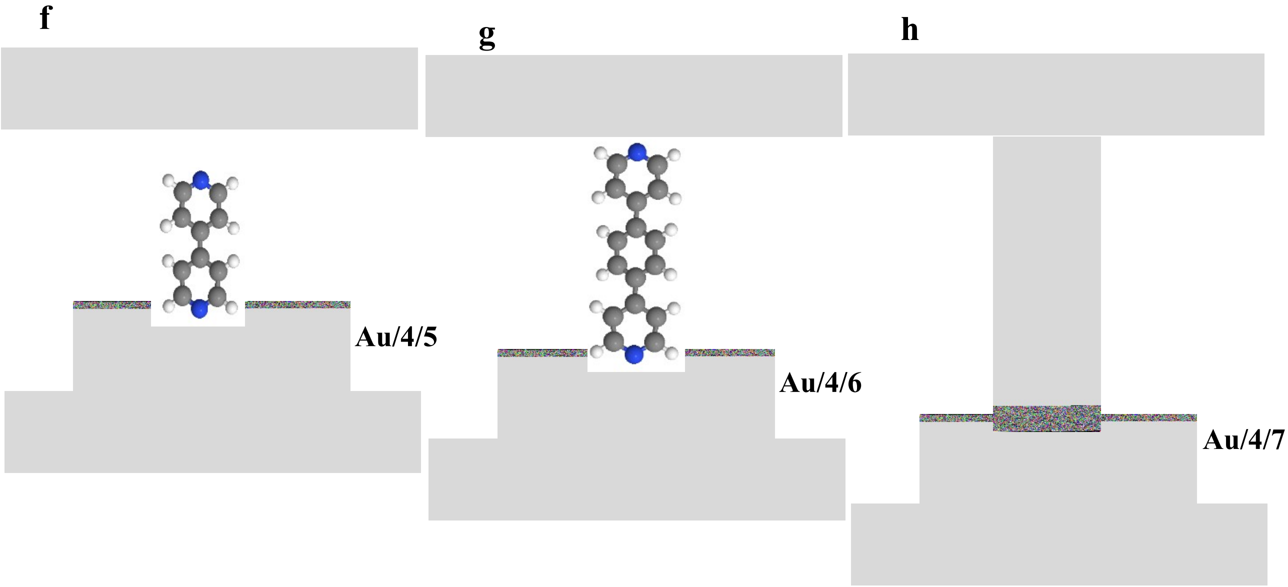

Figure S20: Schematic illustration of the Au/mono-bilayer/Au junctions. Both contacts are Au electrodes. **a-e:** Au/**1-4**/Au monolayer junctions. **f-h:** Au/**4+5-6**/Au bilayer junctions.

1.4.2 Gold-graphene simulations

Here, we repeat the same gold-gold simulations, however, this time single layer of graphene as a top electrode as shown in Fig. S21.

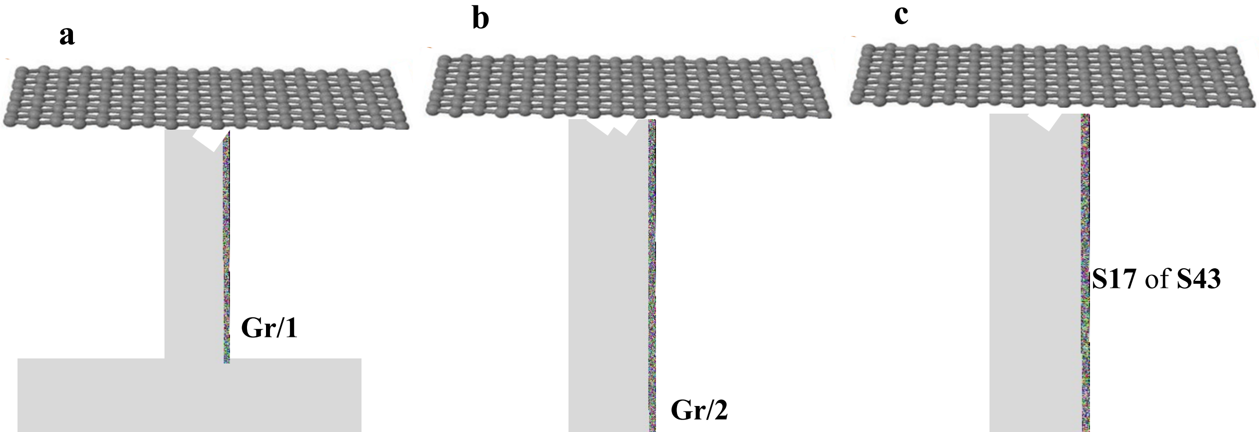

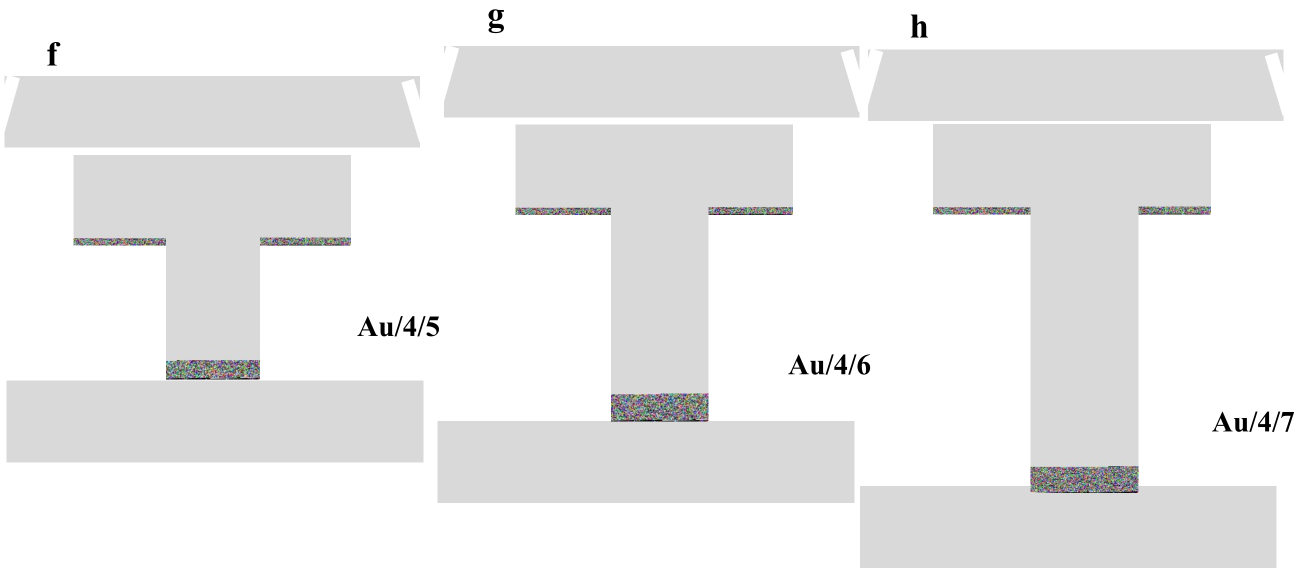

Figure S21: Schematic illustration of the Au/mono-bilayer/SLG junctions. Top contact is SLG electrode and the bottom contact is Au electrode. **a-e:** Au/**1-4**/Au monolayer junctions. **f-h:** Au/**4+5-6**/SLG bilayer junctions.

1.5 Transport Simulation

In the following transport calculations, the ground state Hamiltonian and optimized geometry of each compound was obtained using the density functional theory (DFT) code. The local density approximation (GGA) exchange correlation functional was used along with double zeta polarized (DZP) basis sets and the norm conserving pseudo potentials. The real space grid was defined by a plane wave cut-off of 250 Ry. The geometry optimization was carried out to a force tolerance of 0.01 eV/Å. This process was repeated for a unit cell with the molecule between two electrodes where the optimized distance between electrodes and the anchor groups are shown in Table S1. From the ground state Hamiltonian, the transmission coefficient, the room temperature electrical conductance G was obtained, as described in the sections below. In this section, we shall calculate the transport in different junctions and as follows:

1.5.1 Transport Simulation in Au-Au Junction

1.5.1.1 monolayers 1-3

Based on the binding energy simulations (see Table S1), the transmission coefficient T(E) calculates for Au/**1-3**/Au junctions (see Fig. S20 a-c), as shown in Fig. S22. Transmission coefficients T(E) of Gr and **4** are shown in Figs. S23 and S24 respectively. Since **4** involves a metal atom (Zn), then spin polarisation calculations are required, see Fig. S24.

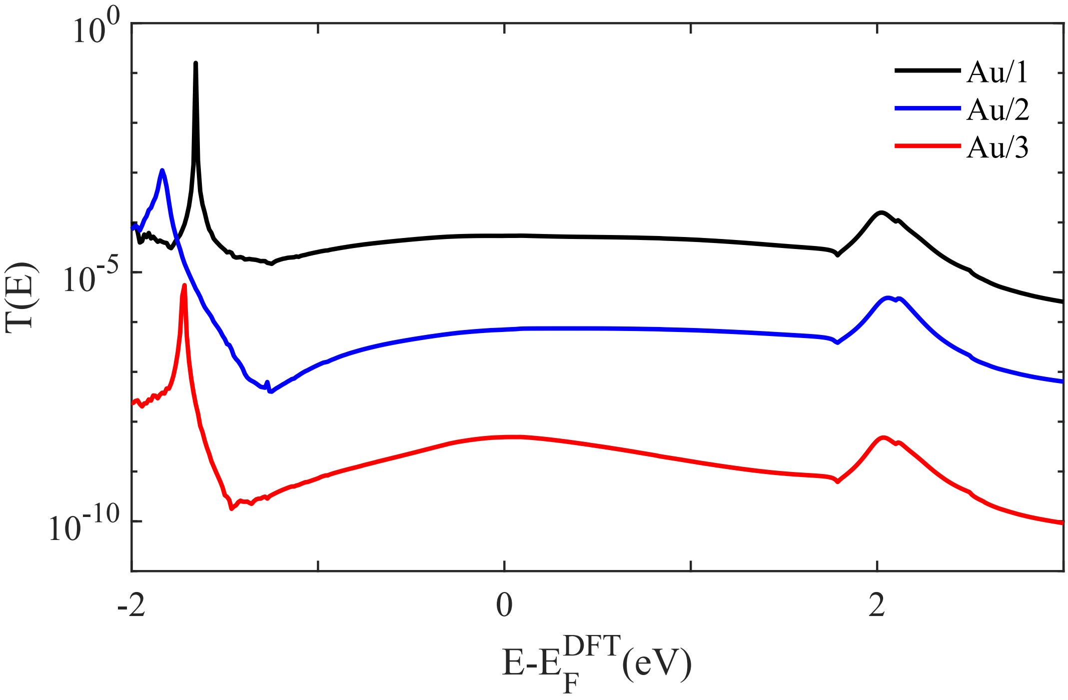

Figure S22: Zero-bias transmission coefficients *T(E)* curves of Au/**1-3**/Au junctions against electron energy E. Monobilayers **1-3,** black, blue and red curves respectively.

1.5.1.2 monolayer Gr

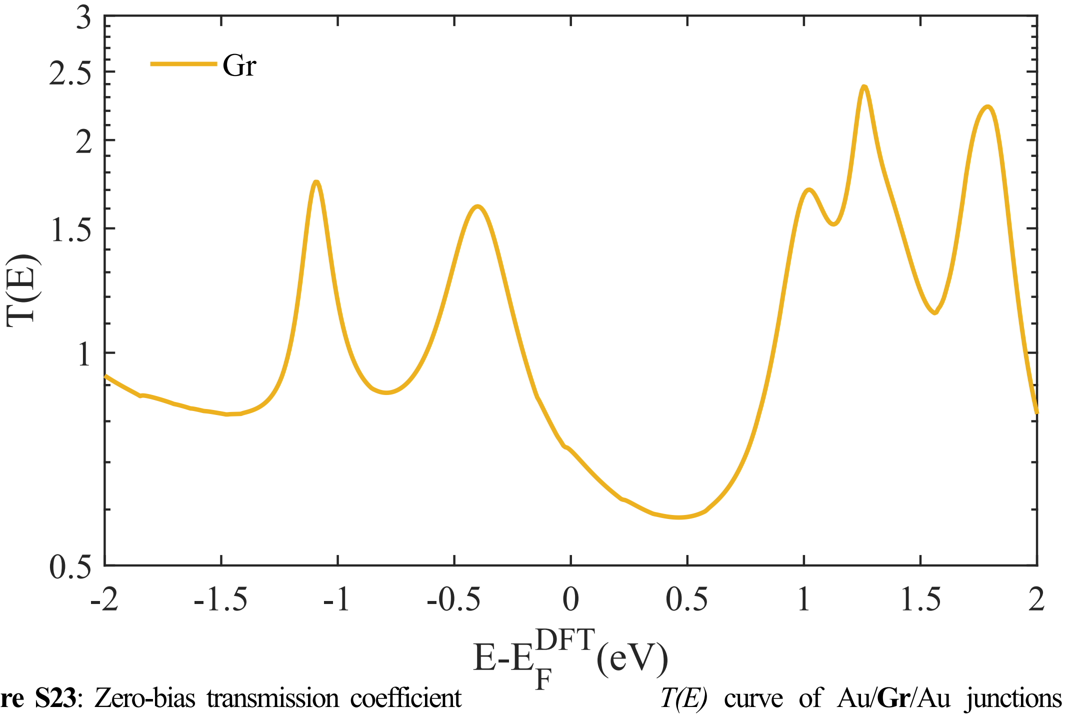

Figure S23: Zero-bias transmission coefficient *T(E)* curve of Au/**Gr**/Au junctions against electron energy E.

1.5.1.3 monolayer 4

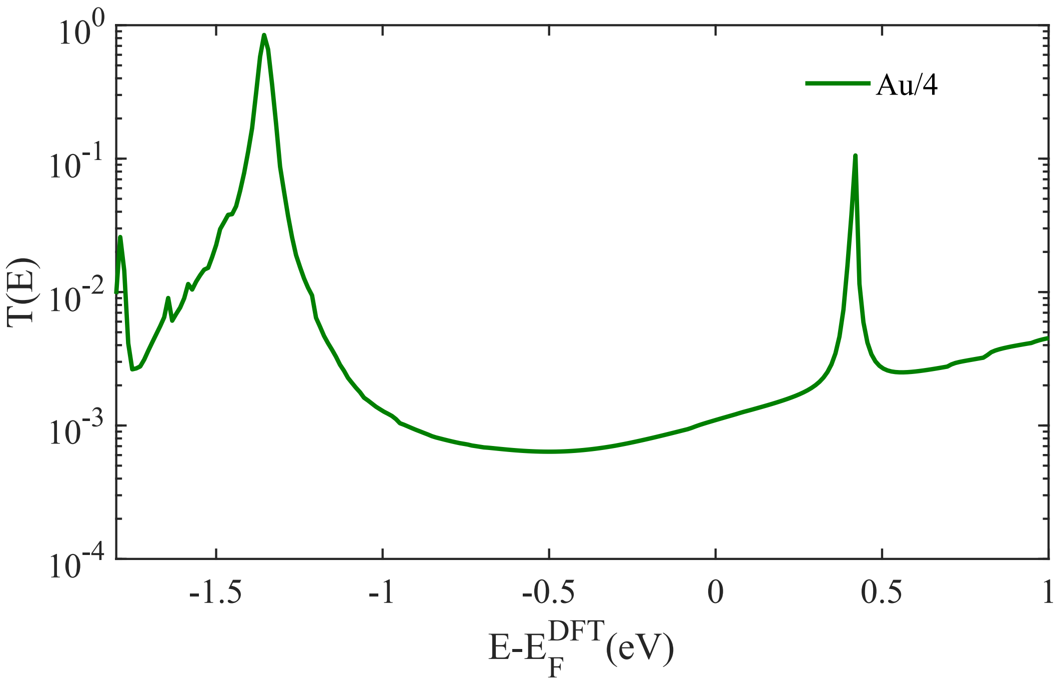

Figure S24: Zero-bias transmission coefficients *T(E)* curve of Au/**4**/Au junctions against electron energy E. Monolayers **4.**

1.5.1.4 bilayer 1

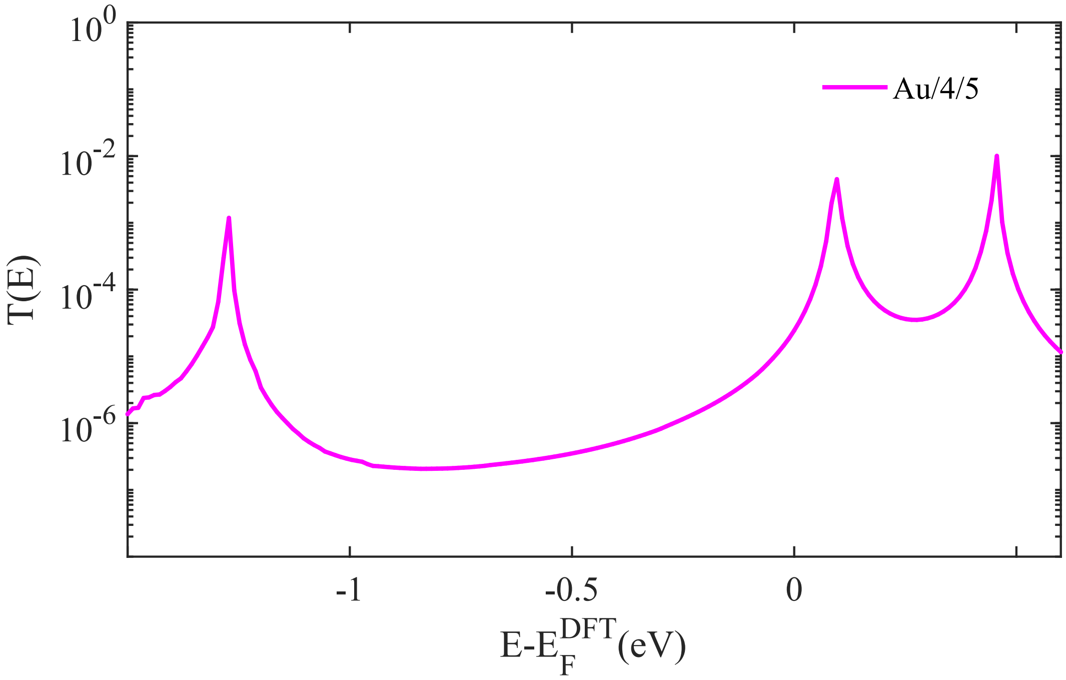

Figure S25: Zero-bias transmission coefficients *T(E)* curve of Au/**4**/**5**/Au junctions against electron energy E. bilayers **1.**

1.5.1.5 bilayer 2

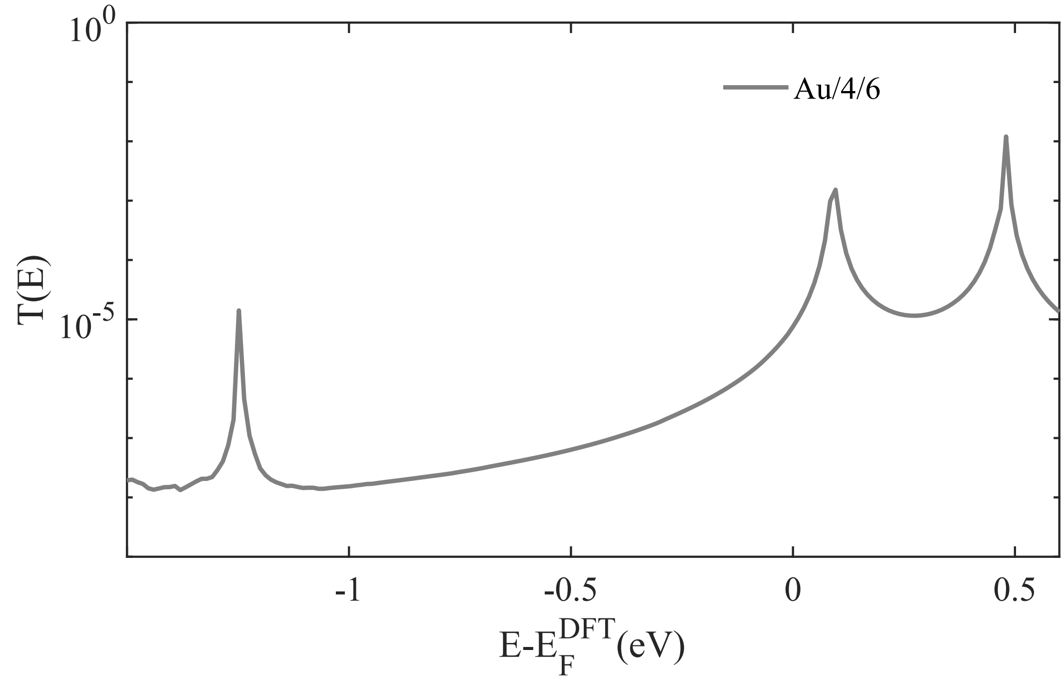

Figure S26: Zero-bias transmission coefficients *T(E)* curve of Au/**4**/**6**/Au junctions against electron energy E. bilayers **2.**

1.5.1.6 bilayer 3

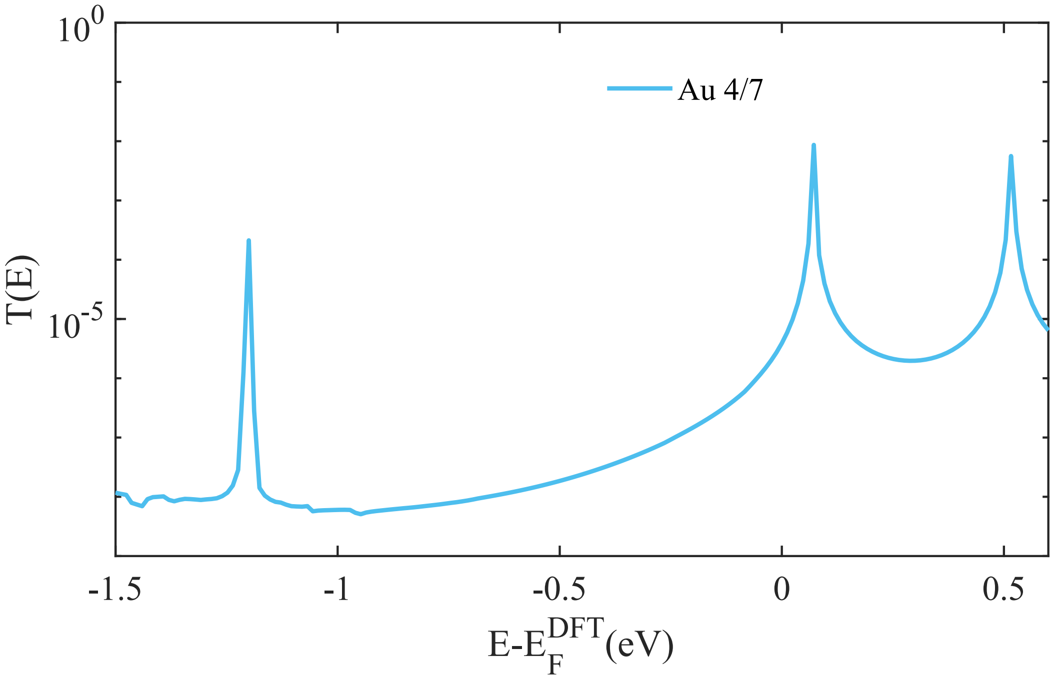

Figure S27: Zero-bias transmission coefficients *T(E)* curve of Au/**4/7**/Au junctions against electron energy E. bilayers **3**.

1.5.2 Transport Simulation in SLG-Au Junction

1.5.2.1 monolayers 1-3

Based on the binding energy simulations (see Table S1), the transmission coefficient T(E) calculates for SLG/**1-3**/Au junctions (see Fig. S21 a-c), as shown in Fig. S28. Transmission coefficients T(E) of Gr and **4** are shown in Figs. S29 and S30 respectively. Since **4** involves a metal atom (Zn), then spin polarisation calculations are required, see Fig. S30.

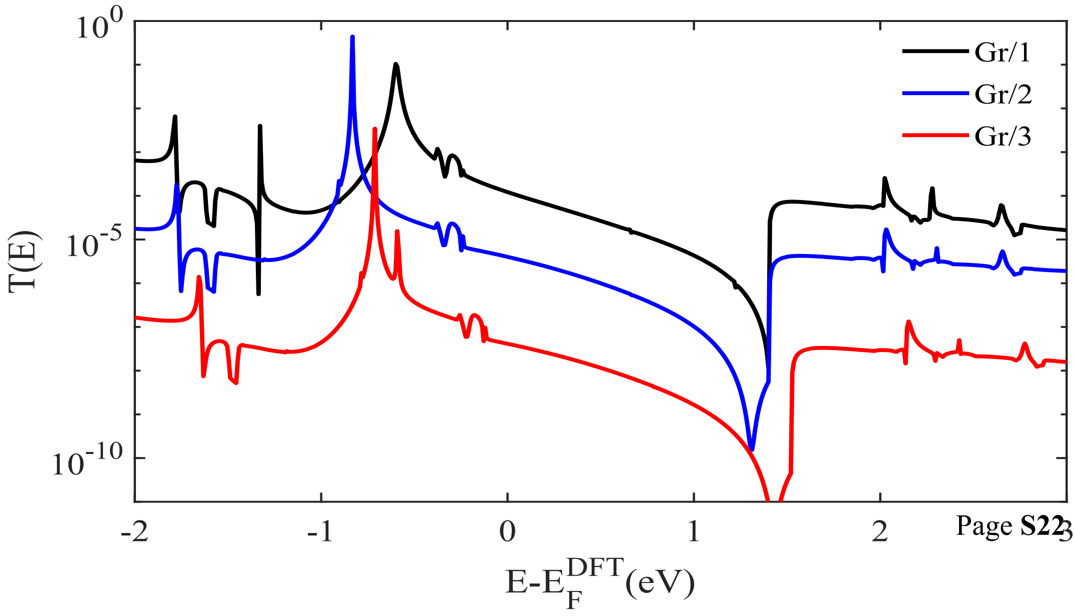

Figure S28: Zero-bias transmission coefficients *T(E)* curves of SLG/**1-3**/Au junctions against electron energy E. Monolayers **1-3,** black, blue and red curves respectively.

1.5.2.2 monolayer Gr

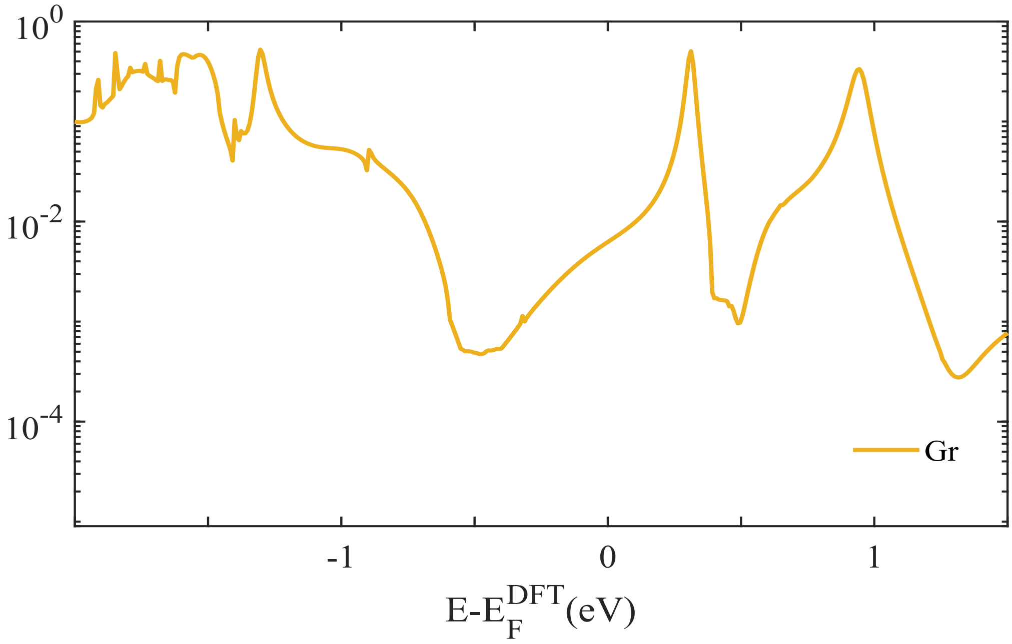

Figure S29: Zero-bias transmission coefficients *T(E)* curves of SLG/**1-3**/Au junctions against electron energy E. Monolayers **Gr,** orang curve.

1.5.2.3 monolayer 4

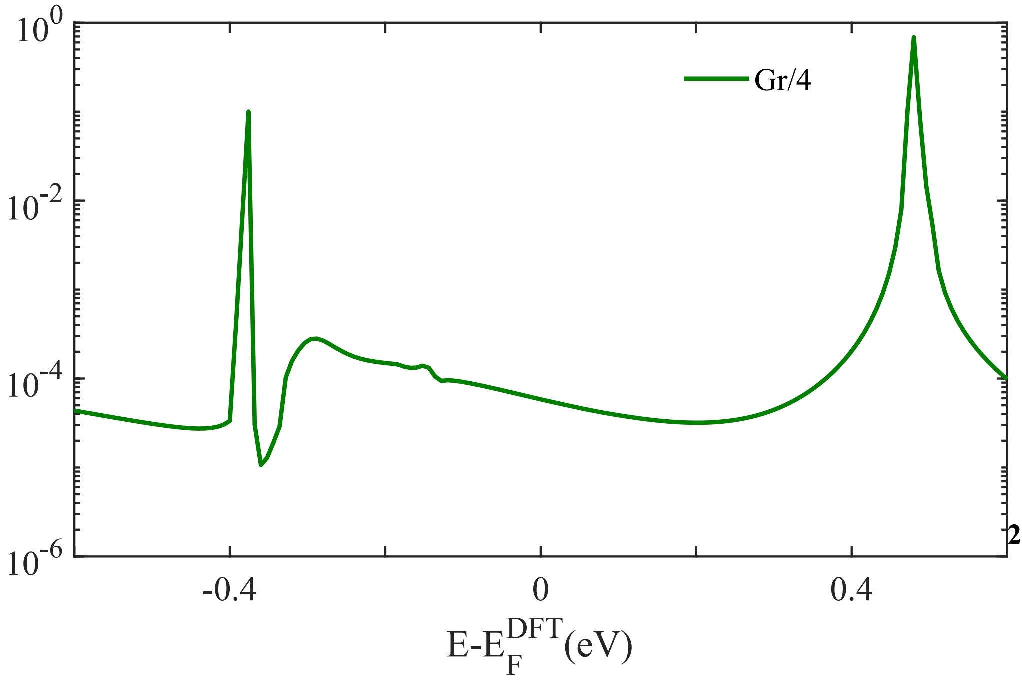

Figure S30: Zero-bias transmission coefficients *T(E)* curve of SLG/**4**/Au junctions against electron energy E. Monolayers **2**.

1.5.2.4 bilayer 1

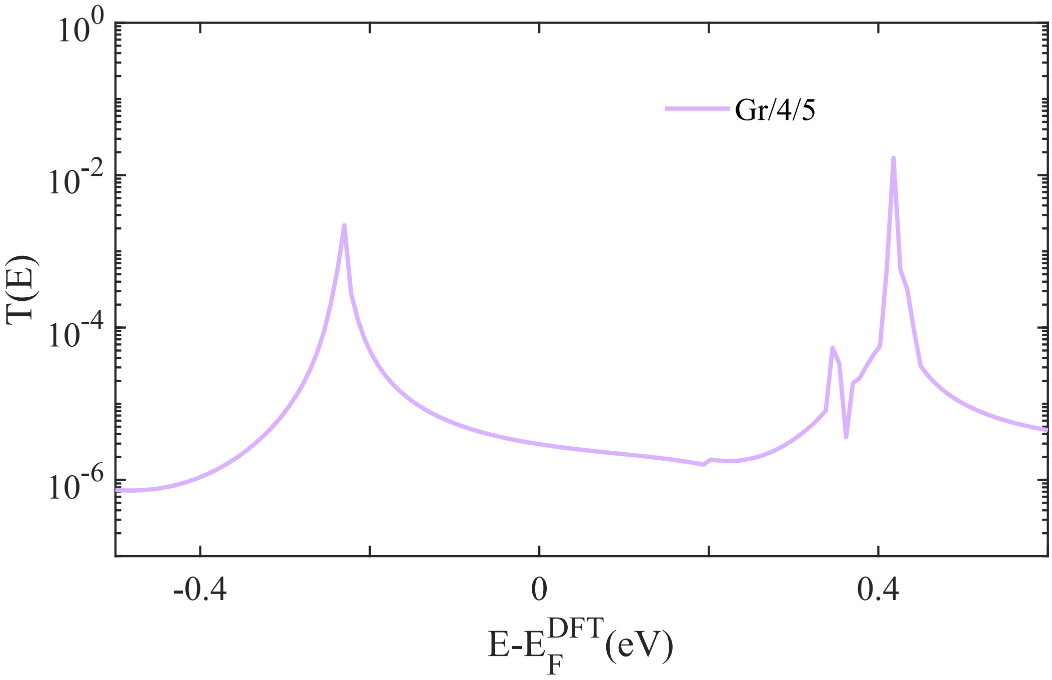

Figure S31: Zero-bias transmission coefficients *T(E)* curve of SLG/**4/5**/Au junctions against electron energy E. Bilayers **1**.

1.5.2.5 bilayer 2

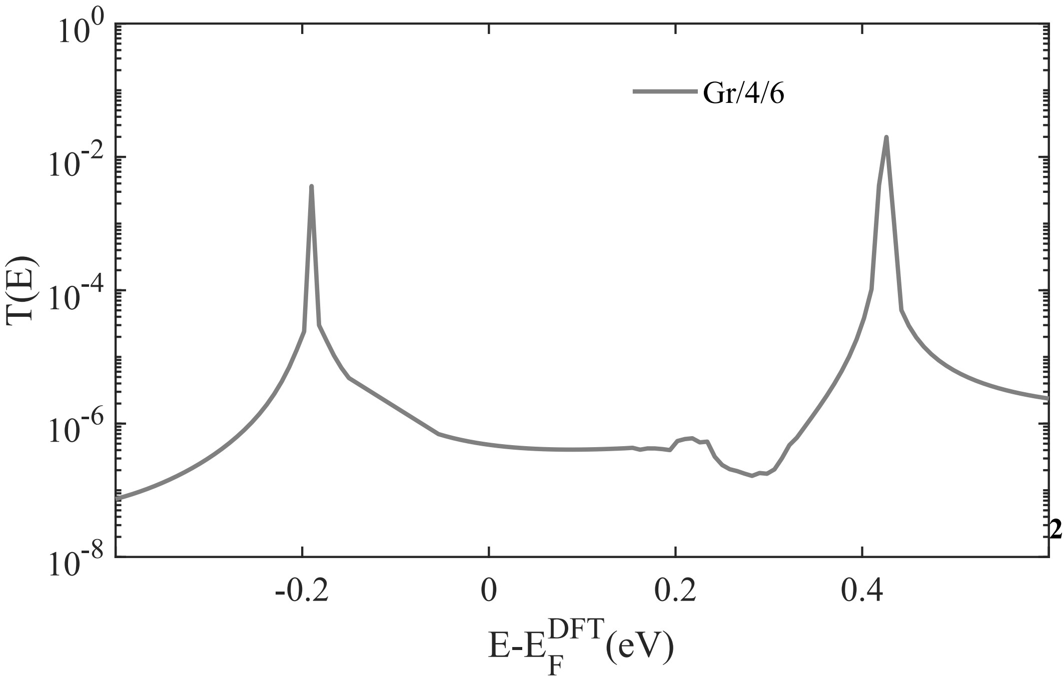

Figure S32: Zero-bias transmission coefficients *T(E)* curve of SLG/**4**/**6**/Au junctions against electron energy E. Bilayers **2**.

1.5.2.6 bilayer 3

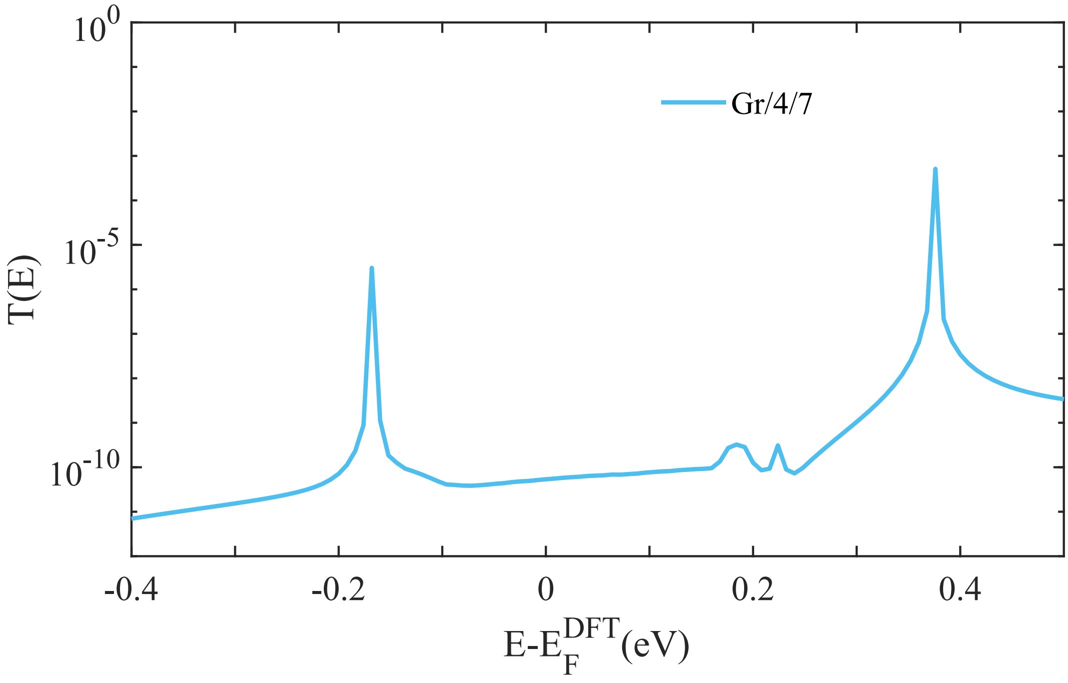

Figure S33: Zero-bias transmission coefficients *T(E)* curve of SLG/**4**/**6**/Au junctions against electron energy E. Bilayers **2**.

1.6 Thermopower Simulation

To calculate the thermopower of the studied molecular junctions, it is useful to introduce the non-normalised probability distribution $P(E)$ defined by

$$P(E) =- T(E)\frac{df(E)}{dE} \tag{S2}$$

where $f(E)$ is the Fermi-Dirac function and $T(E)$ is the transmission coefficients and whose moments L_i are denoted as follows

$$L_i = \int dEP(E)(E - E_F)^i \tag{S3}$$

where E_F is the Fermi energy. The Seebeck coefficient, S, is then given by

$$S(T) =- \frac{1}{eT}\frac{L_1}{L_0} \qquad \text{(S4)}$$

where e is the electronic charge.

The formula evaluated by Gollum code is

$$S^e(T) = \frac{-1}{eT}\frac{L_1}{L_0}$$

where

$$L_i = \int dEP(E)(E-E_F)^i$$

and

$$P(E) =- T(E)\frac{df(E)}{dE}$$

For bilayers, we use expression, $T(E) = \frac{T_{up}(E) + T_{down}(E)}{2}$, where $T_{up}(E)$ and $T_{down}(E)$ are transmission coefficients for the separate spin channels and it is assumed that there is no spin-flip scattering. This equation describes the linear response regime and is consistent with Onsager reciprocal relations. Again, we shall calculate the Seebeck coefficient in two different junctions including Au-Au and SLG-Au.

1.6.1 Thermopower Simulation in Au-Au Junction

1.6.1.1 monolayers 1-4, Gr

Figures S34-S36 show the Seebeck coefficients S of monolayers evaluated at room temperature for different monolayers involving **1, 2, 3**, Gr and **4**.

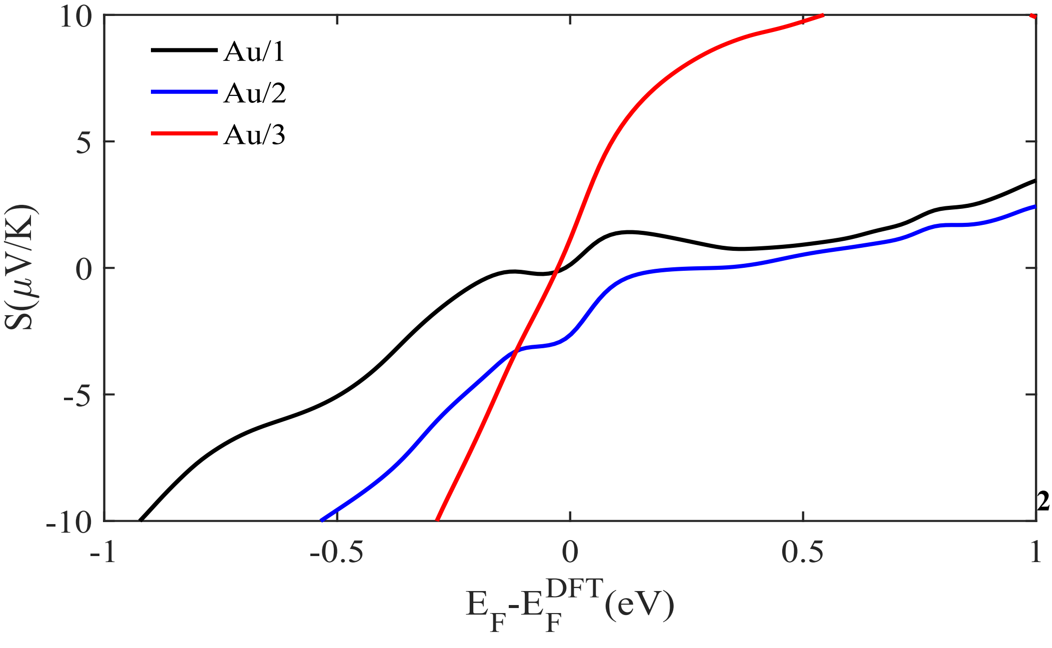

Figure S34: Seebeck coefficient S as a function of Fermi energy of three alkyl chain. Seebeck coefficients of monolayers **1, 2** and **3,** black, blue and red curves respectively.

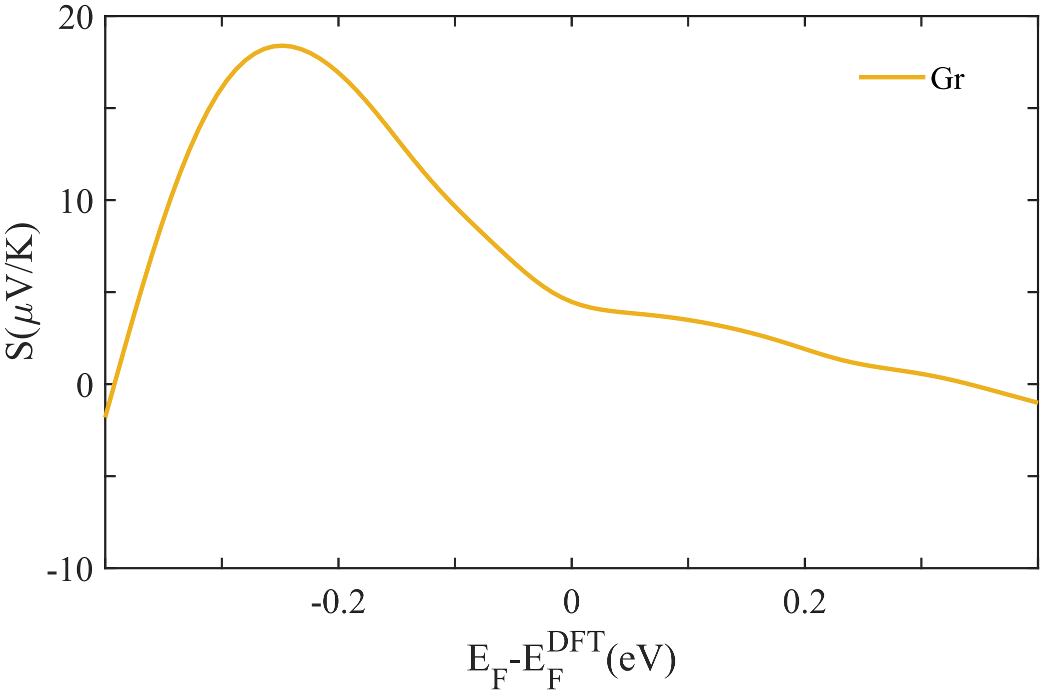

Figure S35: Seebeck coefficient S as a function of Fermi energy of graphene sheet. Seebeck coefficient of monolayer **Gr,** orange curve.

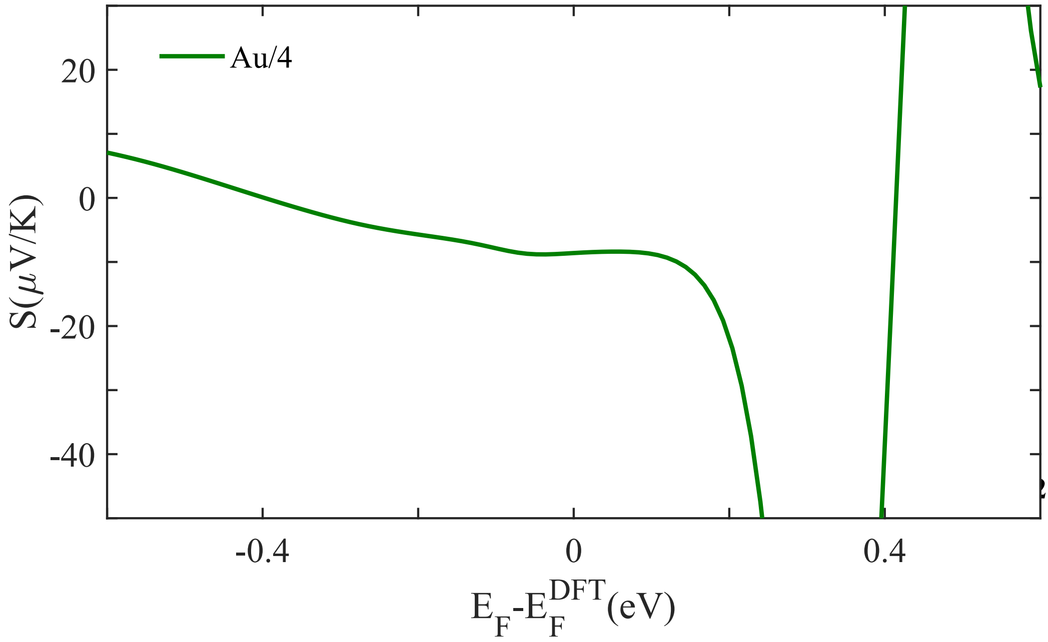

Figure S36: Seebeck coefficient S as a function of Fermi energy of ZnTTP. Seebeck coefficients of monolayer **4,** dark green curve.

1.6.1.2 bilayers 4/5, 4/6 and 4/7

Figures S37-S39 show the Seebeck coefficients S of bilayers evaluated at room temperature for different bilayers involving **4/5, 4/6** and **4/7**.

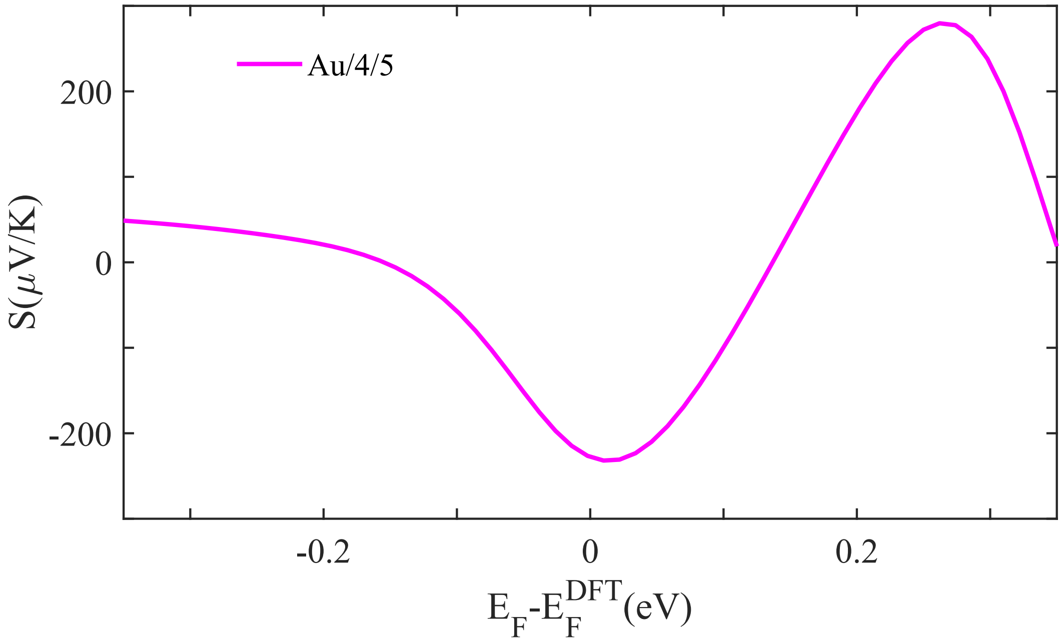

Figure S37: Seebeck coefficient S as a function of Fermi energy of bilayer **1**. Seebeck coefficients of bilayer **4/5,** dark purple curve.

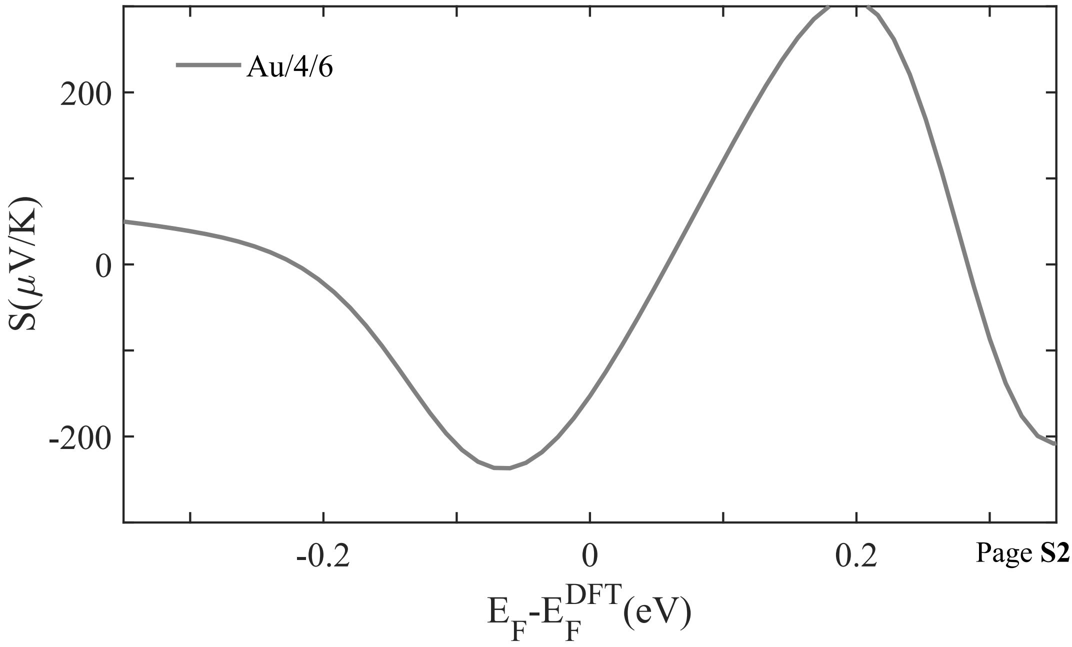

Figure S38: Seebeck coefficient S as a function of Fermi energy of bilayer **2**. Seebeck coefficients of bilayer **4/6,** dark grey curve.

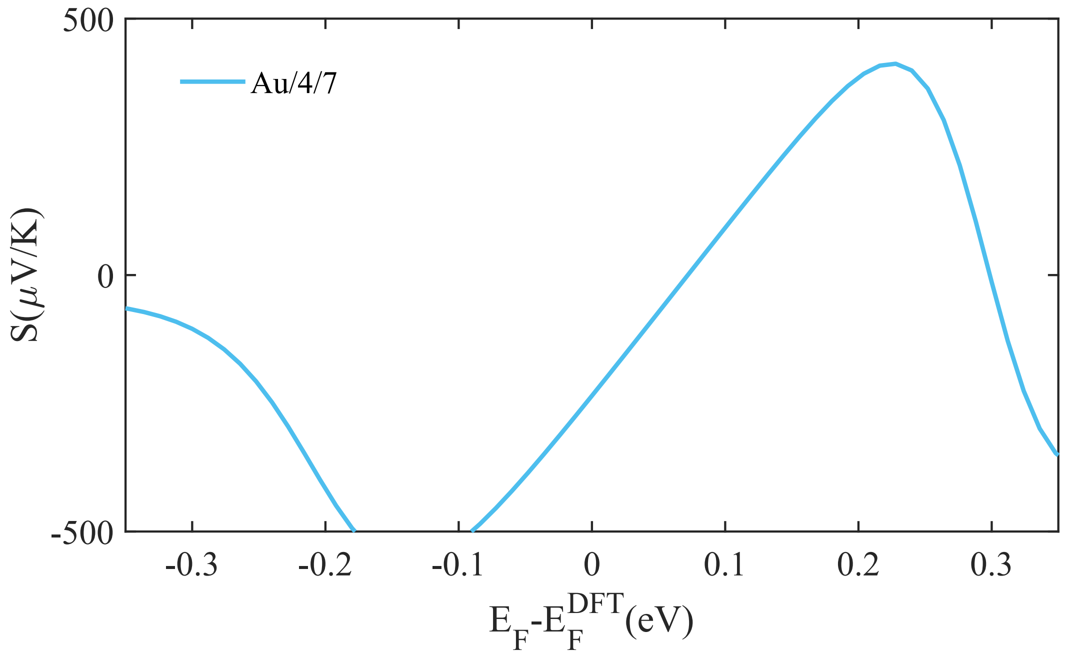

Figure S39: Seebeck coefficient S as a function of Fermi energy of bilayer **3**. Seebeck coefficients of bilayer **4/7,** light blue curve.

1.6.2 Thermopower Simulation in SLG-Au Junction

1.6.2.1 monolayers 1-4, Gr

We shall repeat the same simulation of section 1.6.1 (Au-Au junction), however, this time with Gr-Au junction. Figures S40-S42 show the Seebeck coefficients S of monolayers evaluated at room temperature for different monolayers involving **1, 2, 3**, Gr and **4**.

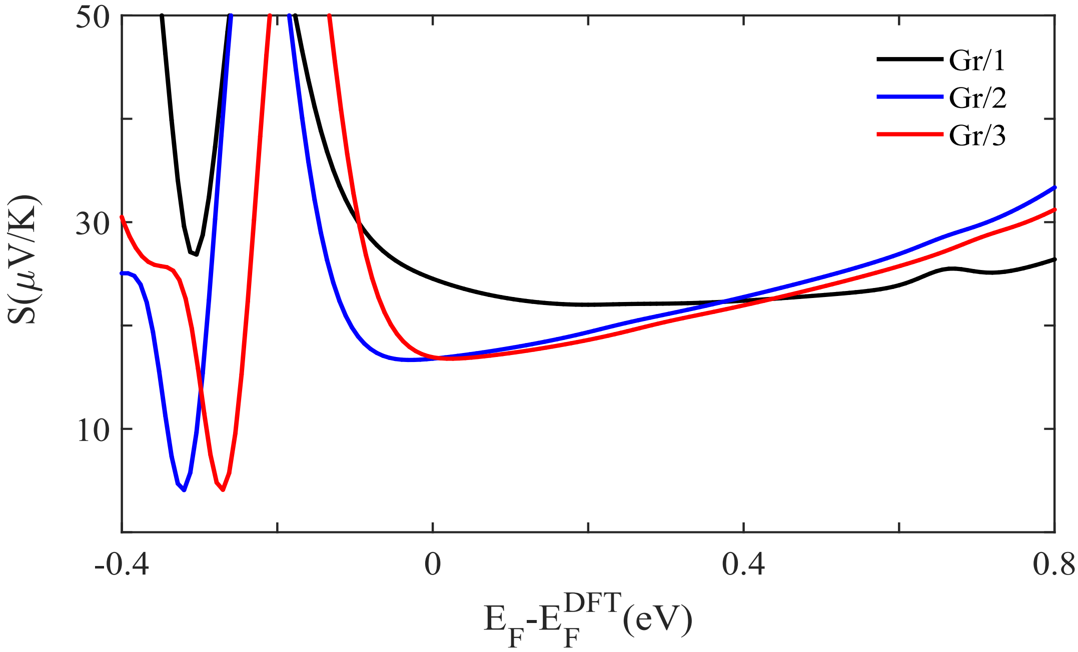

Figure S40: Seebeck coefficient S as a function of Fermi energy of three alkyl chain. Seebeck coefficients of monolayers **1, 2** and **3,** black, blue and red curves respectively.

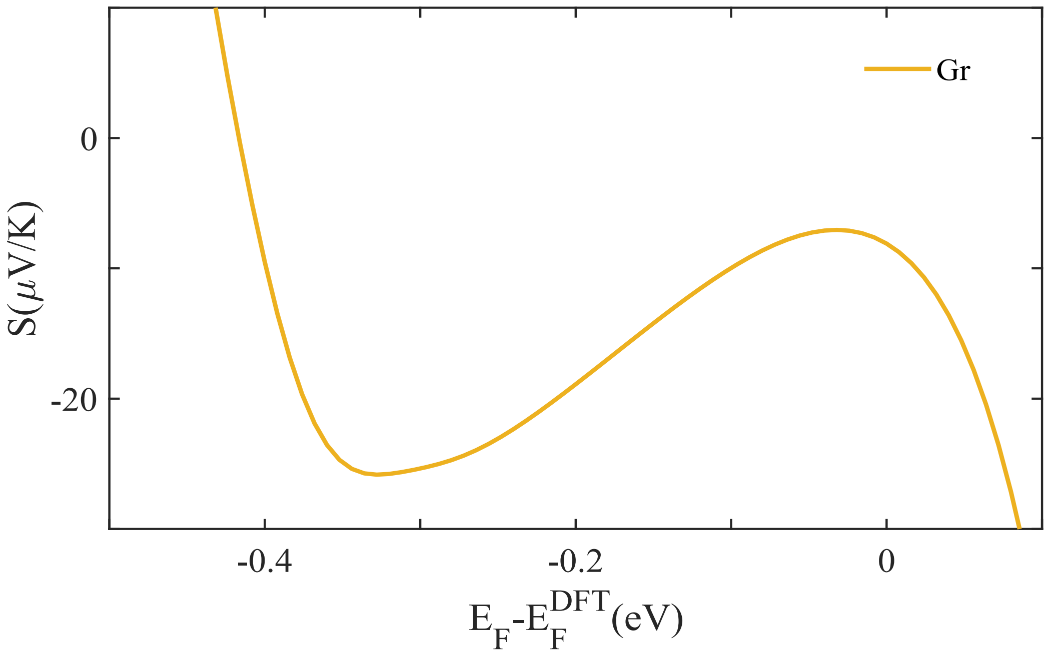

Figure S41: Seebeck coefficient S as a function of Fermi energy of graphene sheet. Seebeck coefficient of monolayer **Gr,** orange curve.

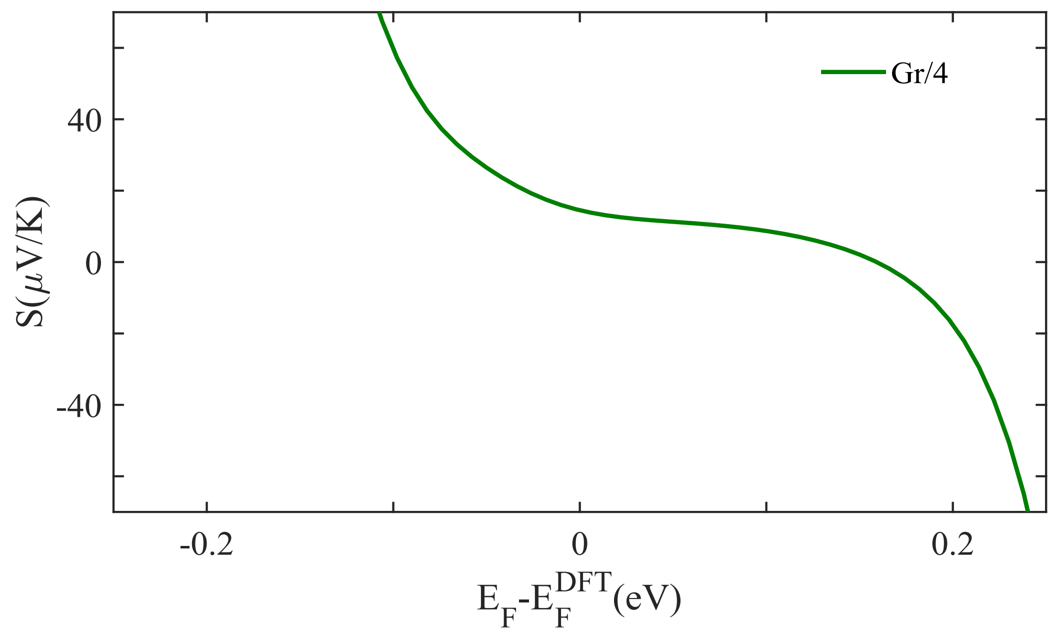

Figure S42: Seebeck coefficient S as a function of Fermi energy of ZnTTP. Seebeck coefficients of monolayer **4,** dark green curve.

1.6.2.2 bilayers 4/5, 4/6 and 4/7

Figures S43-S45 show the Seebeck coefficients S of bilayers evaluated at room temperature for different bilayers involving **4/5, 4/6** and **4/7**.

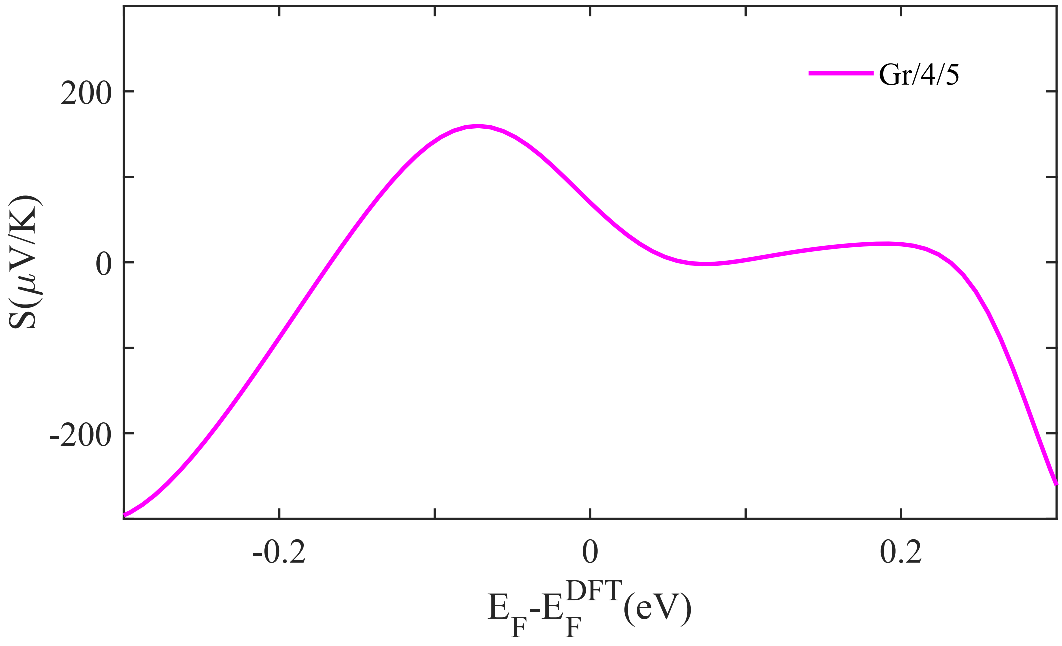

Figure S43: Seebeck coefficient S as a function of Fermi energy of bilayer **1**. Seebeck coefficients of bilayer **4/5,** purple curve.

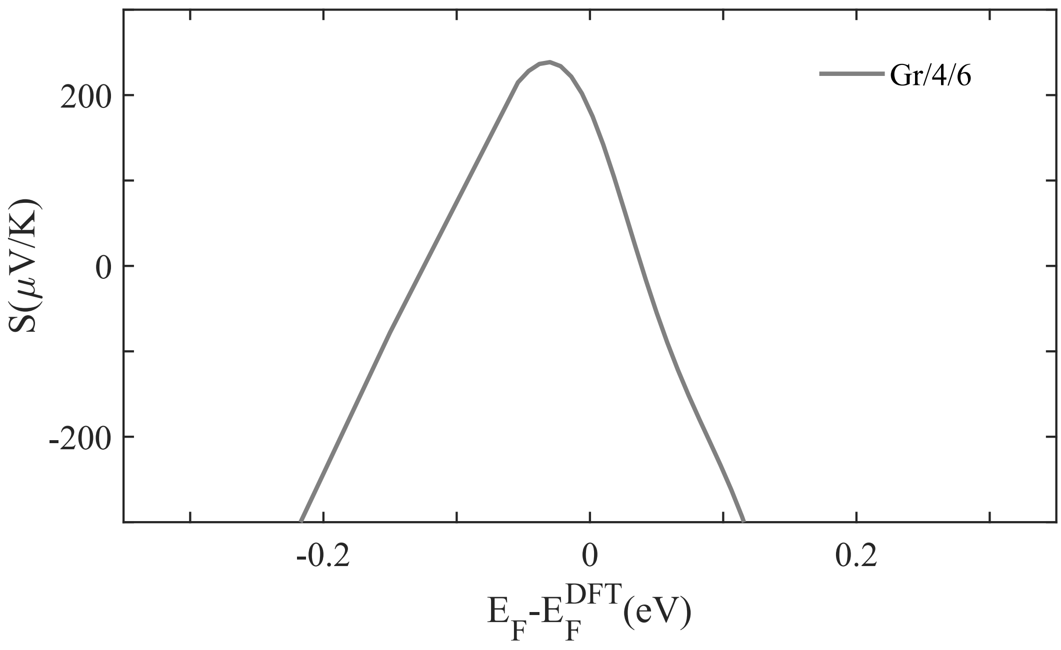

Figure S44: Seebeck coefficient S as a function of Fermi energy of bilayer **2**. Seebeck coefficients of bilayer **4/6,** dark grey curve.

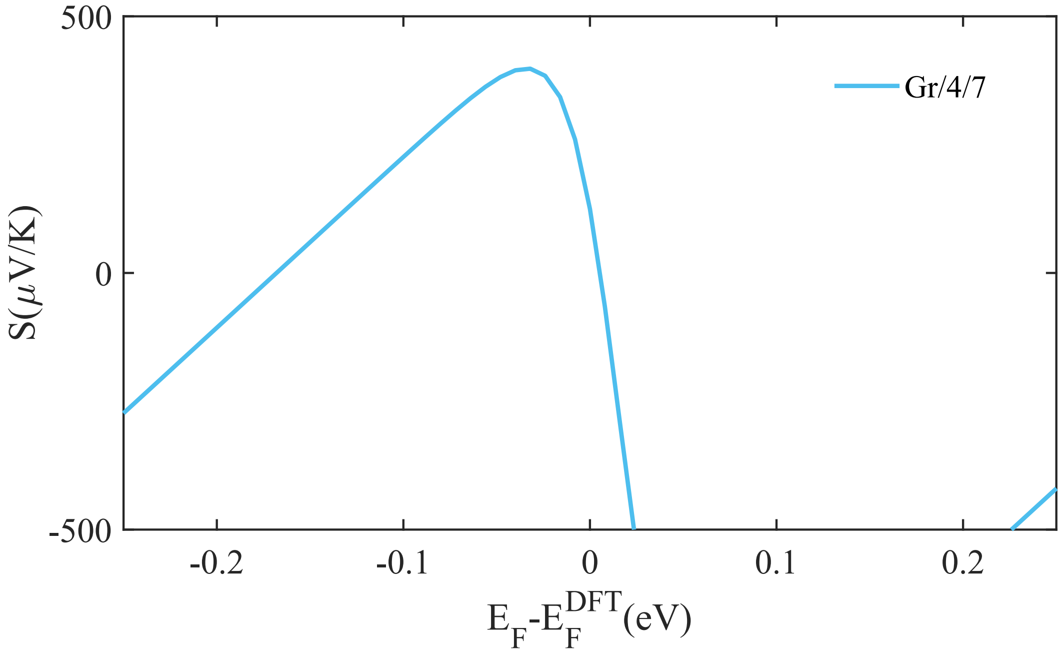

Figure S45: Seebeck coefficient S as a function of Fermi energy of bilayer **3**. Seebeck coefficients of bilayer **4/7,** light blue curve.

Table S2, summarises a comparison between two DFT junctions, mainly Au-Au and Gr-Au, then compare their Seebeck coefficients against the STM measured values for the 8 junctions.

Table S2. Thermoelectric properties of the studied junctions. Measured and calculated Seebeck coefficients STM, and DFT respectively. Simulations at the DFT-predicted Fermi ($E_F - E_F^{DFT} = 0\ eV$), for both Au-Au and Gr-Au junctions

Compound	STM S (µV/K)	Std (µV/K)	DFT Gr/Au S (µV/K)	DFT Au/Au S (µV/K)
Gr/**1**	16.5	8	24	-0.5
Gr/**2**	14	9.5	16.5	-3.0
Gr/**3**	13.5	8	17.0	-1.6
Gr	-0.26	0.2	-8.0	4.0
Gr/**4**	11	4.4	14	-8.0
Gr/**4**/**5**	40	8.4	70	-226
Gr/**4**/**6**	47.5	9.1	178	-235
Gr/**4**/**7**	51	9.2	300	-237

2 Experiment Section:

Graphene Characterization:

Single layered Chemical Vapor Deposited (CVD graphene) graphene were purchased from 6 carbon technology, and the graphene quality was characterized by Raman spectroscopy.

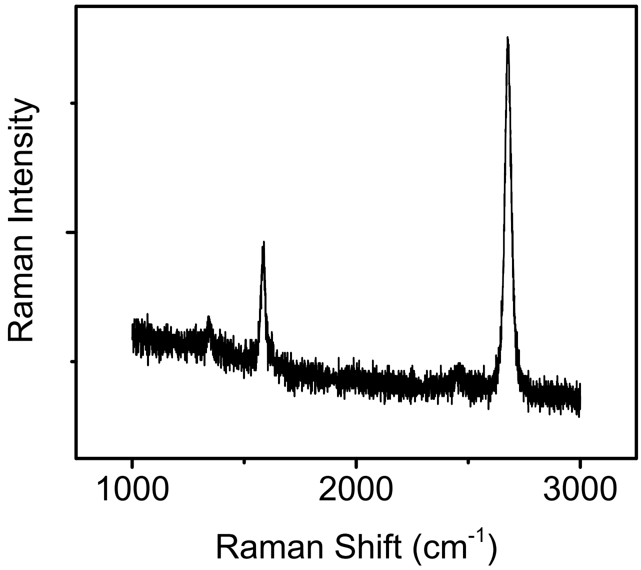

Figure S46: Raman spectra of single layered graphene on copper.

SAMs growth:

SAMs 1-3: Purchased graphene was used for the growth of self-assembled monolayers (SAMs). The growth of SAMs 1-3 (>99%, Aladdin) was carried out following the method published by Song et al. [8].

An 18 mM solution of the target molecule was prepared in a mixed solvent of methanol (>99.9%, Aladdin) and tetrahydrofuran (THF, >99.5%, Aladdin) with a volume ratio of 1:9. The SAMs were grown by immersing the graphene on copper into the solution for 24 hours, followed by rinsing with the mixed solvent three times and drying with a stream of nitrogen.

SAMs 4: A 10 mM solution of SAMs 4 was prepared by dissolving molecule 4 (>98%, Aladdin) in dimethylformamide (DMF, >99.8%, Aladdin) solvent. The graphene on copper was immersed in the solution for 20 minutes, then rinsed with DMF (three times), dichloromethane (DCM, >99.9, Aladdin), and ethanol (>99.5, Sigma Aldrich), and finally dried with a stream of nitrogen.

Coordinating bipyridine molecule: SAMs 4/X (X: 5, 6, 7): 10 mM solutions of molecule 5-7 were prepared by dissolving molecule 5-7 (>95%, Aladdin) in DMF. After the growth of SAMs 4, the graphene was immersed in the solutions of SAMs 5 – 7 for 12 hours to allow for the coordination of pyridine molecules. The resulting SAMs after pyridine coordination were rinsed with DMF (three times), dichloromethane (DCM, >99.9, Aladdin), and ethanol (>99.5, Sigma Aldrich), and finally dried with a stream of nitrogen.

SAMs Characterization: The characterization of self-assembled monolayers (SAMs) on graphene (SAMs 1-3) has been thoroughly conducted and studied by Nijhuis group [9]. The SAMs Gr/4, Gr/4/5, Gr/4/6, and Gr/4/7 were characterized using atomic force microscopy (AFM) and nano-scratching techniques. A tapping mode with a dimension of 3000 and a Multi75-G probe (Budget Sensor) with a force constant of 3 N/m and an apex radius of approximately 10 nm were employed for morphology characterization. Initially, the AFM measurements were performed over a large area to identify defect regions that were not covered by molecules. Subsequently, these defect regions were selected for more detailed scanning (Fig. S47), where the height difference between normal and defect regions provided information about the thickness of the molecular film. It should be noted that most SAMs exhibited defect regions (Fig. S48, arrow region), which were further confirmed by IV measurements showing short circuit curves in certain areas during junction formation.

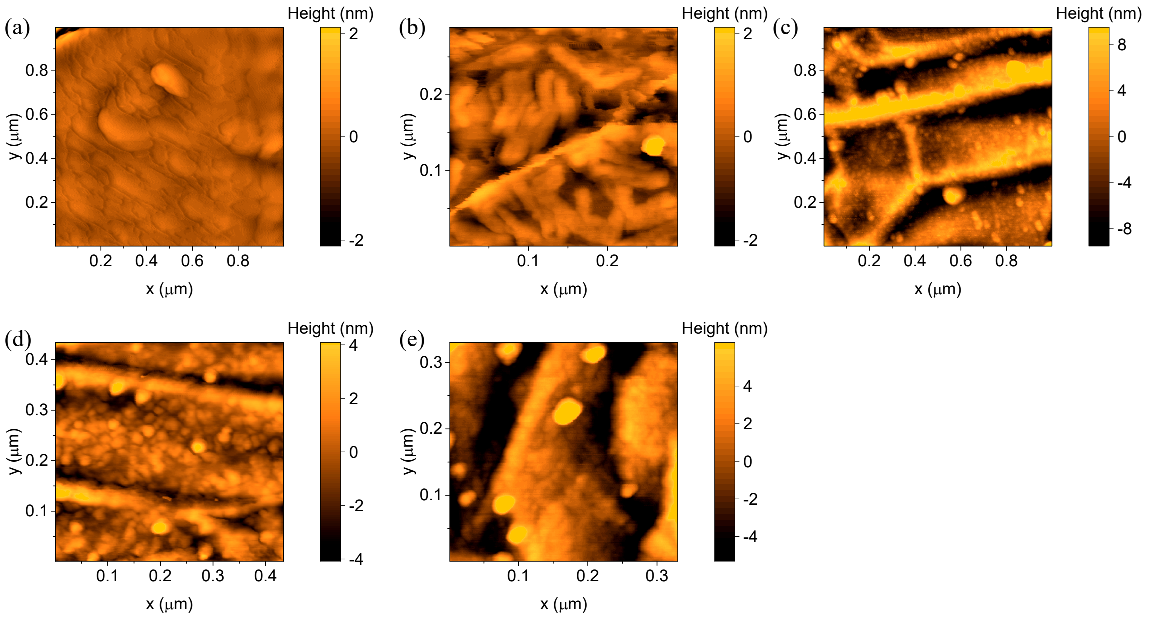

Figure S47: AFM topography image for graphene on copper (a), Gr/4 (b), Gr/4/5 (c), Gr/4/6 (d), Gr/4/7 (e).

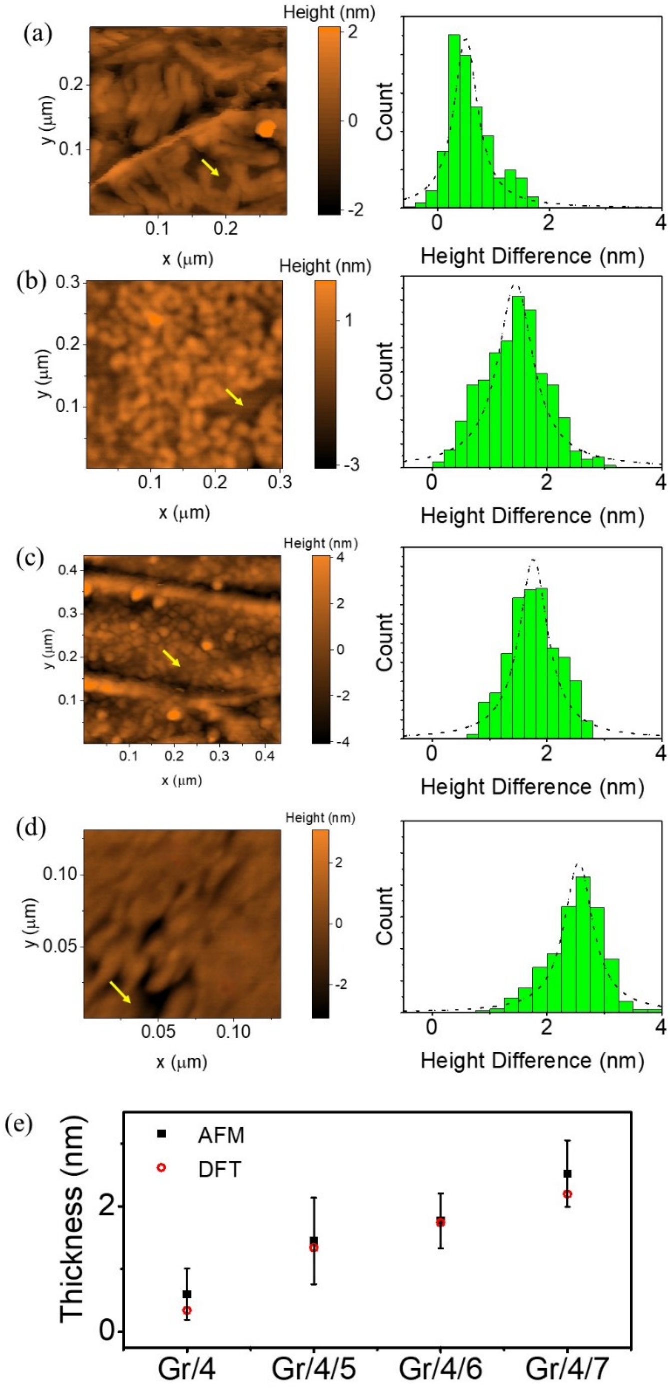

Figure S48 (a-d) (left) AFM topography with yellow arrow point to the defect area. (right) height difference between defect area and normal place using pixel by pixel statistics for Gr/**4**/X SAMs, X: molecule **5-7**. (e) comparison of film thickness between AFM measured result and DFT expected result.

EGaIn tip preparation:

EGaIn tip preparation were according to method published by Ryan *et al* [10]. Eutectic alloy of gallium and indium (>99.99%, Sigma Aldrich) in 10 μL syringe were used for tip preparation. A drop of liquid metal was extruded from the syringe tip (300 μm) and brought into contact with CuO substrate. The cone shapted EGaIn tip with 0.7 nm thick GaOx layer were prepared by slowly retracting syringe

(Figure s1). A micromanipulator (Narishige) were used to control the movement of the tip, and an elevating stage (PDV) was used to control the movement of the sample. A 1600x microscope (Leyue Z04-1) was used to monitor the tip formation procedure.

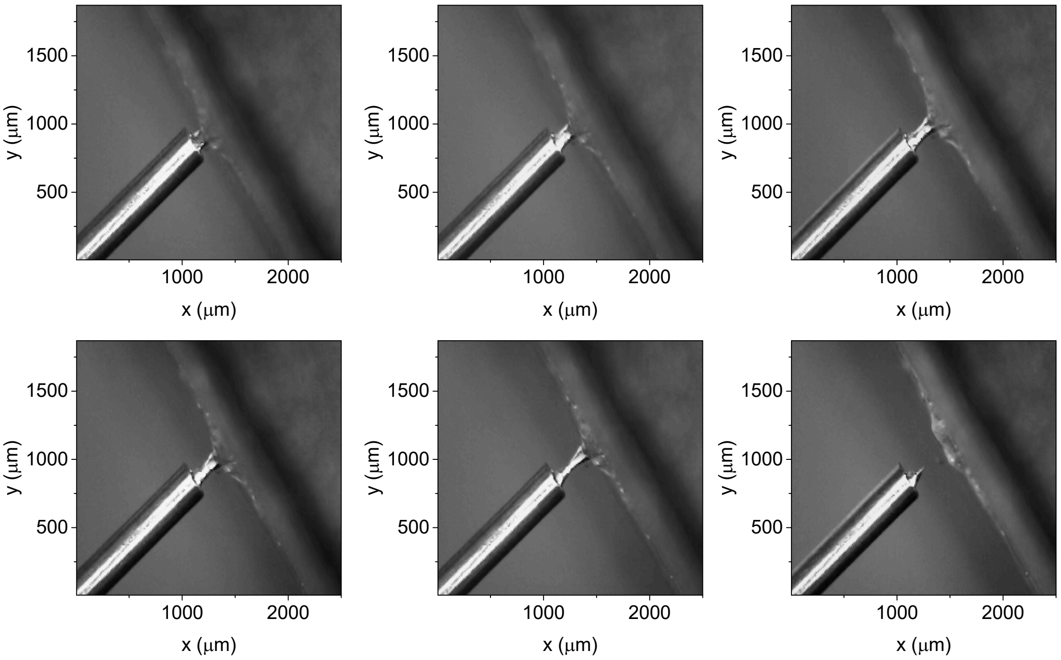

Figure S49: EGaIn tip preparation at ambient condition.

Molecular junction formation:

Graphene sample after SAMs growth were fixed on the peltier stage by scotch tape. The prepared EgaIn tip was brought into contact with SAMs, the contact between tip and sample were monitored by the microscope and the contact area were estimated via the contact radius.

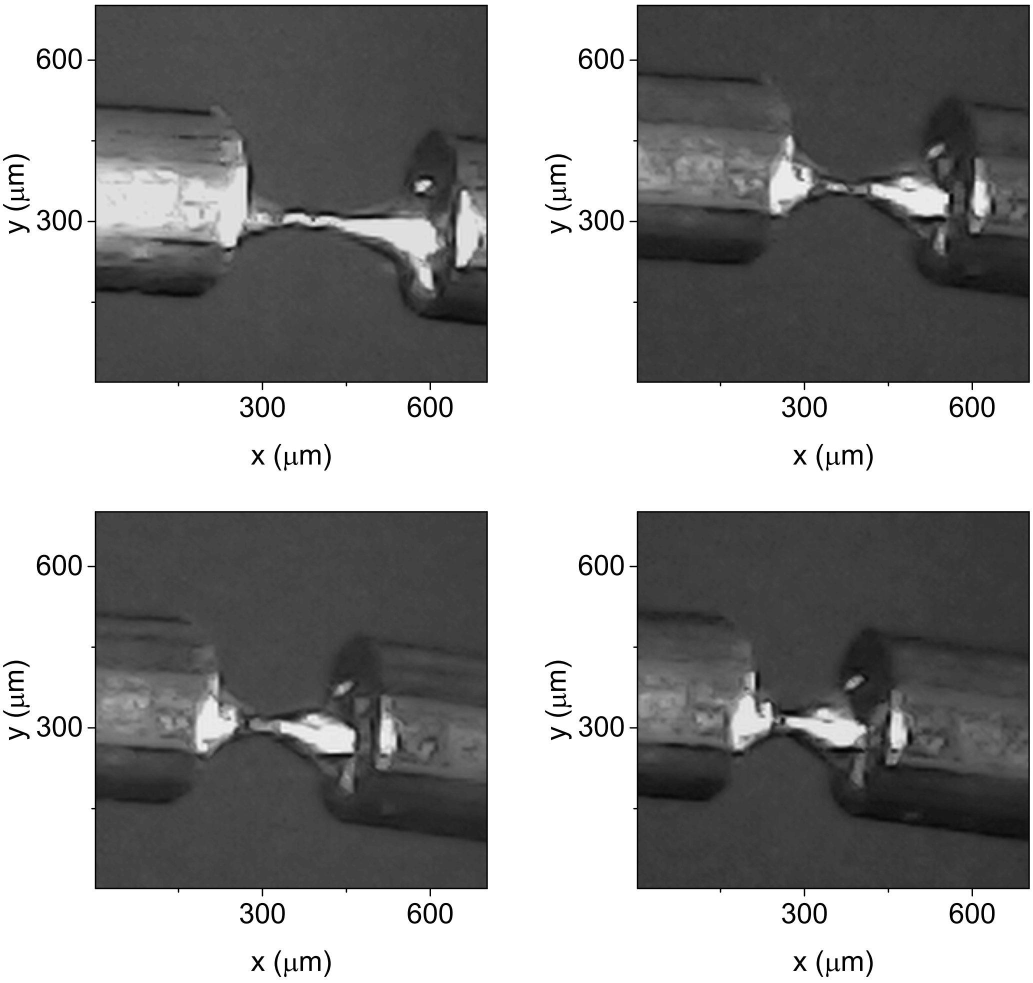

Figure S50: Microscopic image of EGaIn tip gradually push toward sample.

Electric Behaviour Measurement:
A Keithley 2400 source meter was used to characterize the electric behavior of the junction. A bias voltage was added between copper substrate and EgaIn, the current was amplified by a current pre-amplifier (Stanford Research System, SR 570) and collected by a data acquisition card (National Instrument, NI-USB-6295). To avoid the contamination of EGaIn surface by pollutant in air and complicate the contact condition, new tip was freshly prepared for each junction. For each SAMs, at least 80 J - V curves were obtained from at least two independent samples prepared with same method.

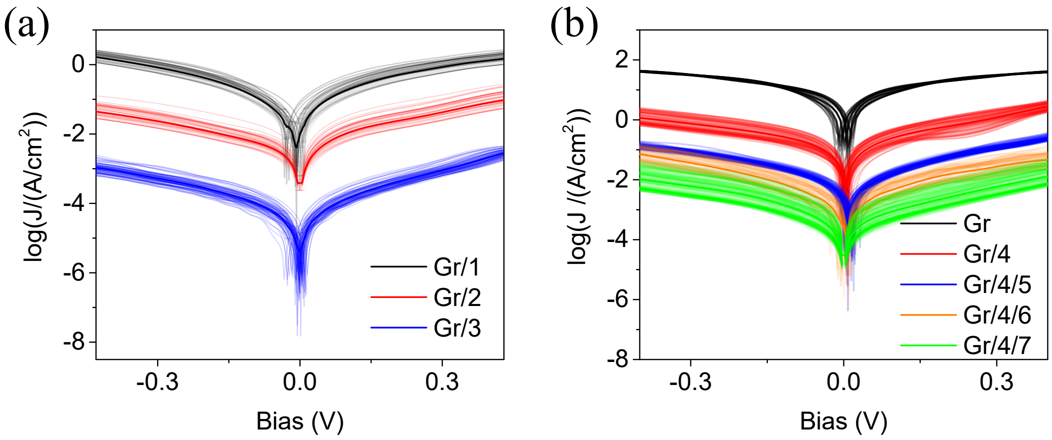

Figure S51: Collected IV curves obtained from all measured junctions.

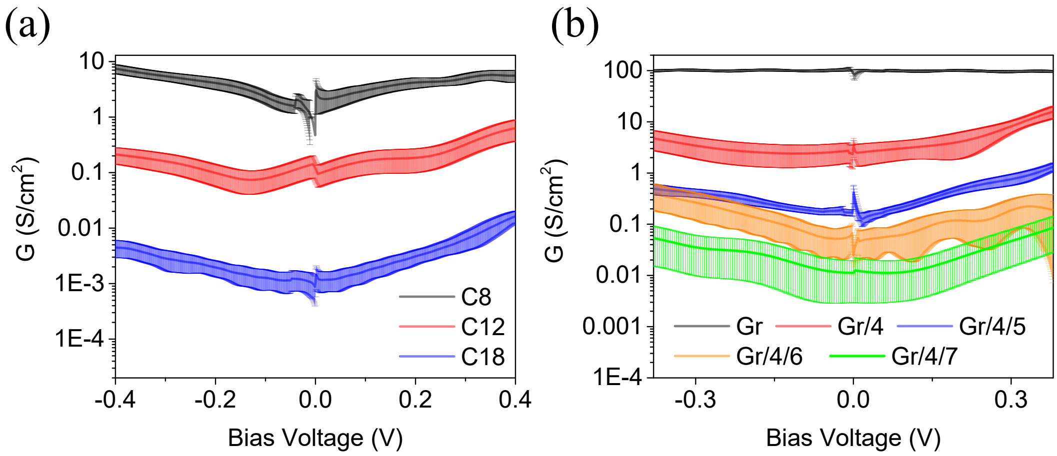

Figure S52: Collected GV curves obtained from all measured junctions, G obtained from numerical differentiation.

Thermoelectric Behaviour Measurement:
A peltier stage was used to create temperature gradient. A thermocouple was used to monitor the temperature on the stage, and another thermocouple was used to monitor the temperature on graphene. The thermos-voltage created between sample and probe was amplified by a low noise voltage pre-amplifier (Stanford Research System, SR560), and recorded by the data acquisition card.

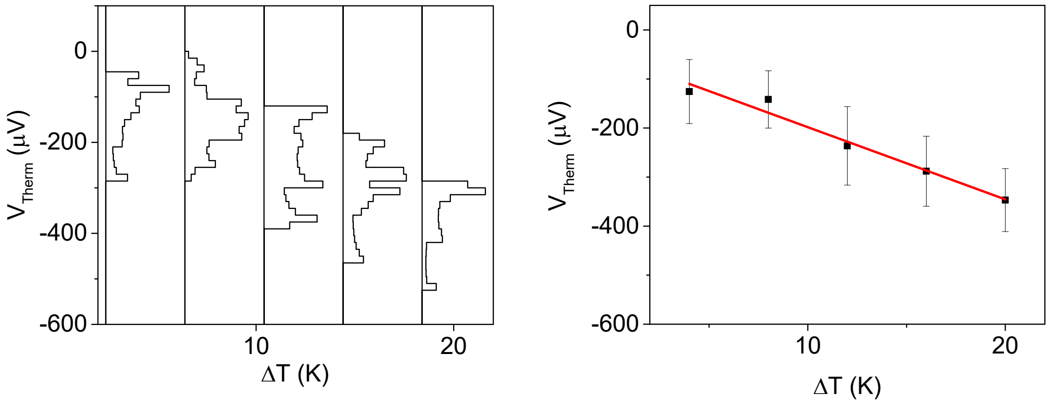

Figure S53: Thermo-voltage of Gr/1 junction at different ΔT, and its linear regression.

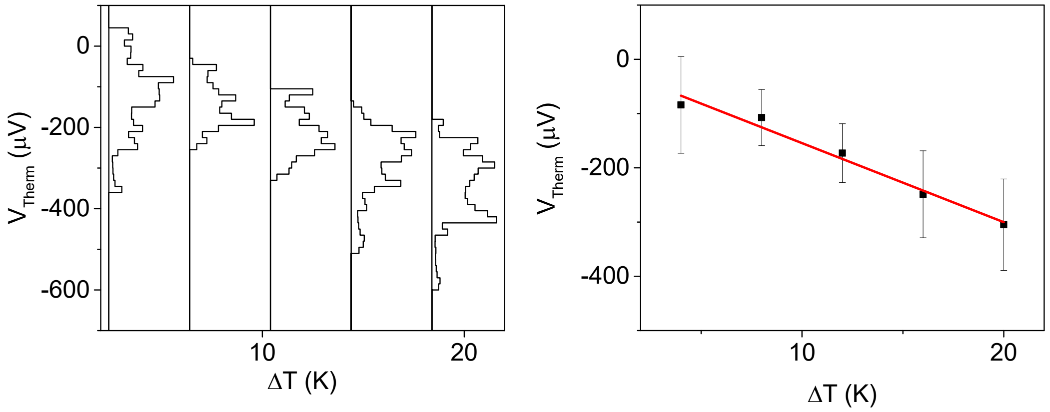

Figure S54: Thermo-voltage of Gr/2 junction at different ΔT, and its linear regression.

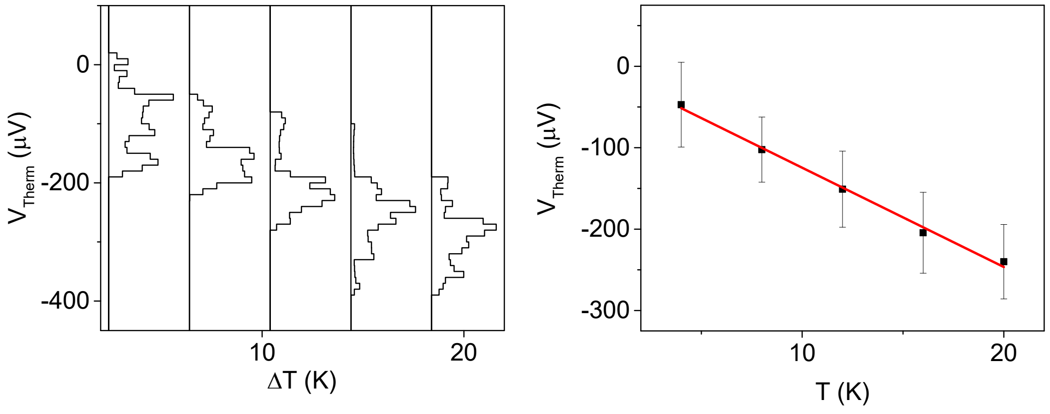

Figure S55: Thermo-voltage of Gr/3 junction at different ΔT, and its linear regression.

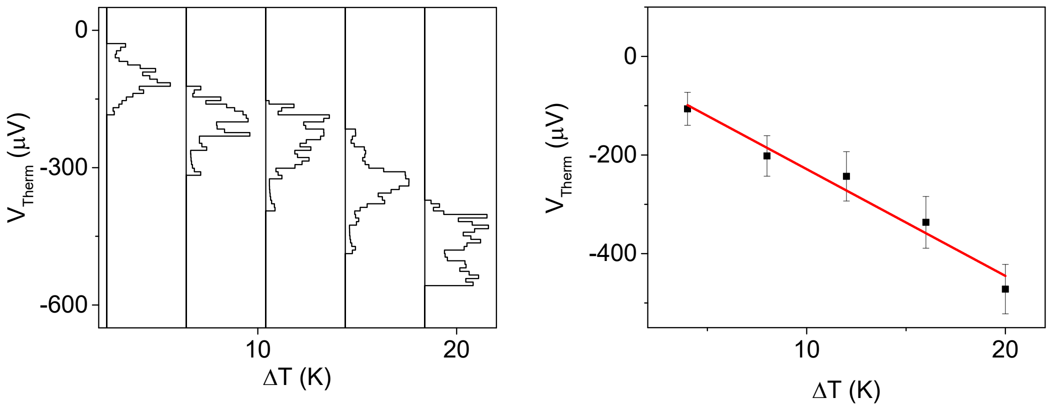

Figure S56: Thermo-voltage of Gr/4 junction at different ΔT, and its linear regression.

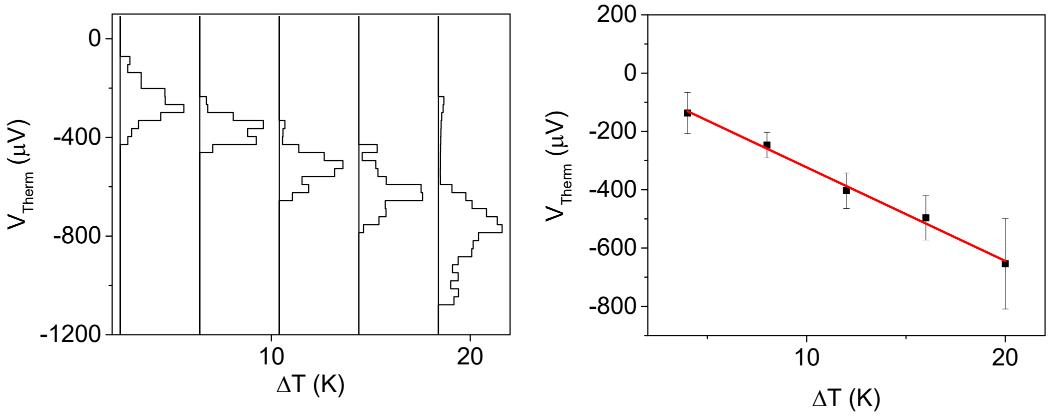

Figure S57: Thermo-voltage of Gr/4/5 junction at different ΔT, and its linear regression.

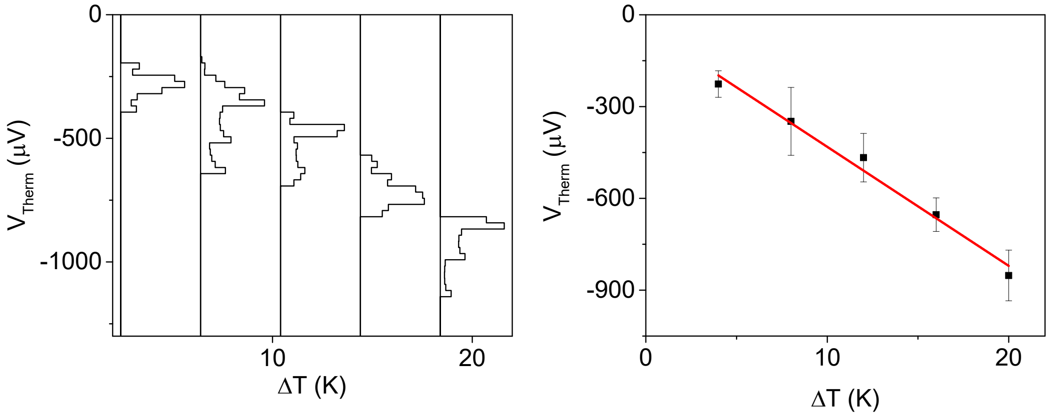

Figure S58: Thermo-voltage of Gr/4/6 junction at different ΔT, and its linear regression.

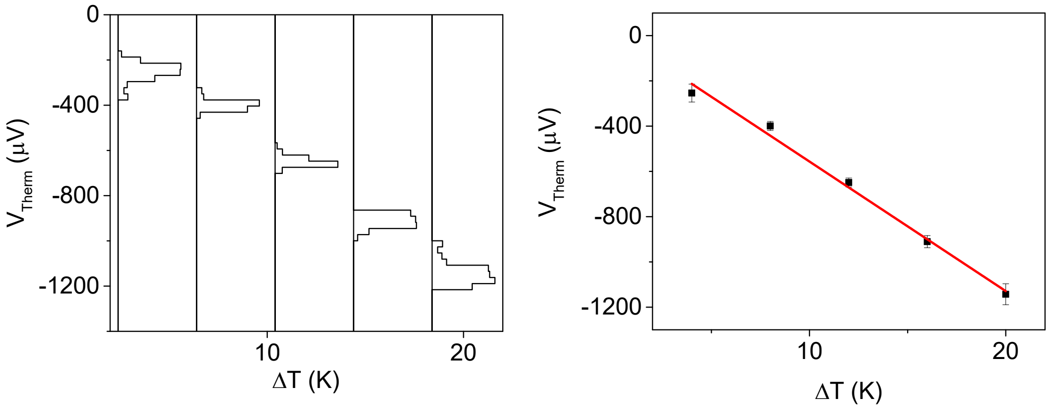

Figure S59: Thermo-voltage of Gr/4/7 junction at different ΔT, and its linear regression.

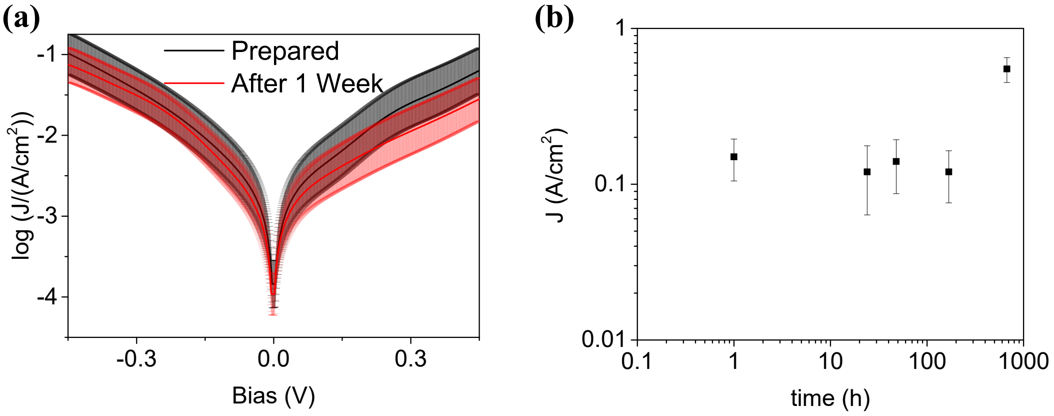

Figure S60: Stability test of Gr/4/X SAMs, (a) JV curve of Gr/4/5 SAMs measured after prepared and leaving in air for 1 week. (b) plot of current density vs. time (in log scale).

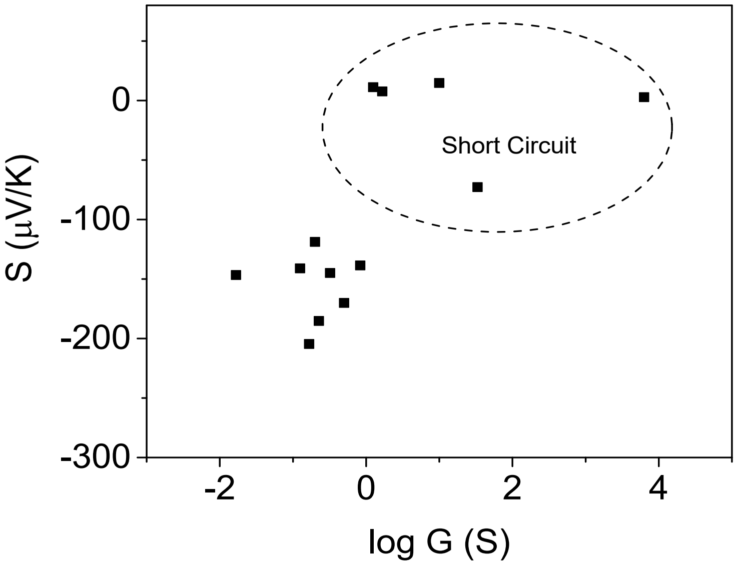

Figure S61: Relationship between Current and Seebeck, V_{therm} obtained at ΔT = 4K.

Table S3: Comparison of molecular junction Seebeck

Electrodes	Molecule	Type	S (uV/K)	Ref
Graphene/EGaIn	CnH2nNH2	SAMs	13.5 to 16.5	This work
Graphene/EGaIn	ZnTPP	SAMs	11	This work
Graphene/EGaIn	ZnTPP/Py(Ph)n	SAMs	40 to 51	This work
Au/Pt	X-DialkynylFerrocene-X	SAMs	-9 to -16.4	[11]
Au/EGaIn	SC3n+1	SAMs	1.5-4.5	[12]
Au/EGaIn	S(EG)nCH3	SAMs	2.2-7.5	[12]
Au/Pt	X-Anthracene core-X	SAMs	-32.8 to 11	[13, 14]
Au/EGaIn	NHC(Ph)n	SAMs	8.1 to 11.5	[15]
Graphene/EGaIn	CnH2n+1NH2	SAMs	10 to 30	[16]
Au/EGaIn	S-(Ph)n-S	SAMs	6.8 to 12	[17]
Au/Pt(or Graphene)	Anthracene-Py/(ZnTPP)	SAMs	-4 to -16	[18]
Au/Au	S-para(meta) OPE -S	SAMs	10.8 to 20.9	[19]
Au/Au	Endohedral Fullerene	single molecule	-31.6 to 25	[20], [21]
Au/Au	S-para OPE3-S	single molecule	8	[22]
Au/Au	S-meta OPE3-S	single molecule	22	[22]
Au/Au	Fullerene	single molecule	-18	[23]
Au/Au	S-(Ph)n-S	single molecule	8 to 13	[22]
Au/Au	S-Oxidized Oligophenyl-S	single molecule	-22.1 to 7.3	[24]
Au/Au	DNA strands	single molecule	0.6 to 7.9	[25]

References

(1) Soler, J. M.; Artacho, E.; Gale, J. D.; García, A.; Junquera, J.; Ordejón, P.; Sánchez-Portal, D. J. J. o. P. C. M. The SIESTA method for ab initio order-N materials simulation. *J. Phys.: Condens. Matter* 2002, *14* (11), 2745.

(2) Perdew, J. P.; Burke, K.; Ernzerhof, M. Generalized gradient approximation made simple. *Phys. Rev. Lett.* 1996, *77* (18), 3865.

(3) Becke, A. D. Density-functional exchange-energy approximation with correct asymptotic behavior. *Phys. Rev. A* 1988, *38* (6), 3098.

(4) Perdew, J. P.; Wang, Y. Accurate and simple analytic representation of the electron-gas correlation energy. *Physical review B* 1992, *45* (23), 13244.

(5) Kobko, N.; Dannenberg, J. Effect of basis set superposition error (BSSE) upon ab initio calculations of organic transition states. *The Journal of Physical Chemistry A* 2001, *105* (10), 1944-1950.

(6) Sherrill, C. D. Counterpoise correction and basis set superposition error. *School of Chemistry and Biochemistry, Georgia Institute of Technology* 2010.

(7) Sinnokrot, M. O.; Valeev, E. F.; Sherrill, C. D. Estimates of the ab initio limit for π− π interactions: The benzene dimer. *Journal of the American Chemical Society* 2002, *124* (36), 10887-10893.

(8) Song, P.; Sangeeth, C. S. S.; Thompson, D.; Du, W.; Loh, K. P.; Nijhuis, C. A. Noncovalent Self-Assembled Monolayers on Graphene as a Highly Stable Platform for Molecular Tunnel Junctions. *Adv Mater* 2016, *28* (4), 631-639. DOI: 10.1002/adma.201504207.

(9) Song, P.; Guerin, S.; Tan, S. J. R.; Annadata, H. V.; Yu, X. J.; Scully, M.; Han, Y. M.; Roemer, M.; Loh, K. P.; Thompson, D.; et al. Stable Molecular Diodes Based on pi-pi Interactions of the Molecular

Frontier Orbitals with Graphene Electrodes. *Adv Mater* 2018, *30* (10). DOI: ARTN 1706322. 10.1002/adma.201706322.

(10) Chiechi, R. C.; Weiss, E. A.; Dickey, M. D.; Whitesides, G. M. Eutectic gallium-indium (EGaIn): A moldable liquid metal for electrical characterization of self-assembled monolayers. *Angewandte Chemie-International Edition* 2008, *47* (1), 142-144. DOI: 10.1002/anie.200703642.

(11) Wilkinson, L. A.; Bennett, T. L. R.; Grace, I. M.; Hamill, J.; Wang, X. T.; Au-Yong, S.; Ismael, A.; Jarvis, S. P.; Hou, S. J.; Albrecht, T.; et al. Assembly, structure and thermoelectric properties of 1,1 '-dialkynylferrocene 'hinges'. *Chem Sci* 2022, *13* (28), 8380-8387. DOI: 10.1039/d2sc00861k.

(12) Cho, N. Y.; Kang, S.; Lee, H.; Kang, H. G.; Kong, G. D.; Yoon, H. J. Superexchange Coupling-Induced Enhancements of Thermoelectric Performance in Saturated Molecules. *Nano Lett* 2021, *21* (1), 360-366. DOI: 10.1021/acs.nanolett.0c03736.

(13) Ismael, A.; Wang, X. T.; Bennett, T. L. R.; Wilkinson, L. A.; Robinson, B. J.; Long, N. J.; Cohen, L. F.; Lambert, C. J. Tuning the thermoelectrical properties of anthracene-based self-assembled monolayers. *Chem Sci* 2020, *11* (26), 6836-6841. DOI: 10.1039/d0sc02193h.

(14) Wang, X. T.; Bennett, T. L. R.; Ismael, A.; Wilkinson, L. A.; Hamill, J.; White, A. J. P.; Grace, I. M.; Kolosov, O. V.; Albrecht, T.; Robinson, B. J.; et al. Scale-Up of Room-Temperature Constructive Quantum Interference from Single Molecules to Self-Assembled Molecular-Electronic Films. *J Am Chem Soc* 2020, *142* (19), 8555-8560. DOI: 10.1021/jacs.9b13578.

(15) Kang, S.; Park, S.; Kang, H.; Cho, S. J.; Song, H.; Yoon, H. J. Tunneling and thermoelectric characteristics of N-heterocyclic carbene-based large-area molecular junctions. *Chem Commun* 2019, *55* (60), 8780-8783. DOI: 10.1039/c9cc01585j.

(16) Park, S.; Kim, H. R.; Kim, J.; Hong, B. H.; Yoon, H. J. Enhanced Thermopower of Saturated Molecules by Noncovalent Anchor-Induced Electron Doping of Single-Layer Graphene Electrode. *Adv Mater* 2021, *33* (41). DOI: ARTN 2103177. 10.1002/adma.202103177.

(17) Park, S.; Yoon, H. J. New Approach for Large-Area Thermoelectric Junctions with a Liquid Eutectic Gallium-Indium Electrode. *Nano Lett* 2018, *18* (12), 7715-7718. DOI: 10.1021/acs.nanolett.8b03404.

(18) Bennett, T. L. R.; Alshammari, M.; Au-Yong, S.; Almutlg, A.; Wang, X. T.; Wilkinson, L. A.; Albrecht, T.; Jarvis, S. P.; Cohen, L. F.; Ismael, A.; et al. Multi-component self-assembled molecular-electronic films: towards new high-performance thermoelectric systems. *Chem Sci* 2022, *13* (18), 5176-5185. DOI: 10.1039/d2sc00078d.

(19) Miao, R. J.; Xu, H. L.; Skripnik, M.; Cui, L. J.; Wang, K.; Pedersen, K. G. L.; Leijnse, M.; Pauly, F.; Warnmark, K.; Meyhofer, E.; et al. Influence of Quantum Interference on the Thermoelectric Properties of Molecular Junctions. *Nano Lett* 2018, *18* (9), 5666-5672. DOI: 10.1021/acs.nanolett.8b02207.

(20) Rincon-Garcia, L.; Ismael, A. K.; Evangeli, C.; Grace, I.; Rubio-Bollinger, G.; Porfyrakis, K.; Agrait, N.; Lambert, C. J. Molecular design and control of fullerene-based bi-thermoelectric materials. *Nat Mater* 2016, *15* (3), 289-+. DOI: 10.1038/Nmat4487.

(21) Lee, S. K.; Buerkle, M.; Yamada, R.; Asai, Y.; Tada, H. Thermoelectricity at the molecular scale: a large Seebeck effect in endohedral metallofullerenes. *Nanoscale* 2015, *7* (48), 20497-20502. DOI: 10.1039/c5nr05394c.

(22) Reddy, P.; Jang, S. Y.; Segalman, R. A.; Majumdar, A. Thermoelectricity in molecular junctions. *Science* 2007, *315* (5818), 1568-1571. DOI: 10.1126/science.1137149.

(23) Evangeli, C.; Gillemot, K.; Leary, E.; Gonzalez, M. T.; Rubio-Bollinger, G.; Lambert, C. J.; Agrait, N. Engineering the Thermopower of C-60 Molecular Junctions. *Nano Lett* 2013, *13* (5), 2141-2145. DOI: 10.1021/nl400579g.

(24) Dell, E. J.; Capozzi, B.; Xia, J. L.; Venkataraman, L.; Campos, L. M. Molecular length dictates the nature of charge carriers in single-molecule junctions of oxidized oligothiophenes. *Nat Chem* 2015, *7* (3), 209-214. DOI: 10.1038/Nchem.2160.

(25) Li, Y. Q.; Xiang, L. M.; Palma, J. L.; Asai, Y.; Tao, N. J. Thermoelectric effect and its dependence on molecular length and sequence in single DNA molecules. *Nat Commun* 2016, *7*. DOI: ARTN 11294. 10.1038/ncomms11294.